# FILTERED POINT PROCESSES TRACTABLY CAPTURE RHYTHMIC AND BROADBAND POWER SPECTRAL STRUCTURE IN NEURAL ELECTROPHYSIOLOGICAL RECORDINGS

**Patrick F. Bloniasz**
Graduate Program for Neuroscience
Boston University
Boston, MA 02215
pblonias@bu.edu

**Shohei Oyama**
Undergraduate Program for Neuroscience
Boston University
Boston, MA 02215

Administration, Leadership, and Technology
New York University
Brooklyn, New York, 10003

**Emily P. Stephen**
Department of Math and Statistics
Boston University
Boston, MA 02215
estephen@bu.edu

## ABSTRACT

Neural electrophysiological recordings arise from interacting rhythmic (oscillatory) and broadband (aperiodic) biological subprocesses. Both rhythmic and broadband processes contribute to the neural power spectrum, which decomposes the variance of a neural recording across frequencies. Although an extensive body of literature has successfully studied rhythms in various diseases and brain states, researchers only recently have systematically studied the characteristics of broadband effects in the power spectrum. Broadband effects can generally be categorized as 1) shifts in power across all frequencies, which correlate with changes in local firing rates and 2) changes in the overall shape of the power spectrum, such as the spectral slope or power law exponent. Shape changes are evident in various conditions and brain states, influenced by factors such as excitation to inhibition balance, age, and various diseases. It is increasingly recognized that broadband and rhythmic effects can interact on a sub-second timescale. For example, broadband power is time-locked to the phase of $<1$ Hz rhythms in propofol induced unconsciousness. Modeling tools that explicitly deal with both rhythmic and broadband contributors to the power spectrum and that capture their interactions are essential to help improve the interpretability of power spectral effects. Here, we introduce a tractable stochastic forward modeling framework designed to capture both narrowband and broadband spectral effects when prior knowledge or theory about the primary biophysical processes involved is available. Population-level neural recordings are modeled as the sum of filtered point processes (FPPs), each representing the contribution of a different biophysical process such as action potentials or postsynaptic potentials of different types. Our approach builds on prior neuroscience FPP work by allowing multiple interacting processes and time-varying firing rates and by deriving theoretical power spectra and cross-spectra. We demonstrate several properties of the models, including that they divide the power spectrum into frequency ranges dominated by rhythmic and broadband effects, and that they can capture spectral effects across multiple timescales, including sub-second cross-frequency coupling. The framework can be used to interpret empirically observed power spectra and cross-frequency coupling effects in biophysical terms, which bridges the gap between theoretical models and experimental results.

Electrical field recordings in the brain – such as local field potentials (LFP), electrocorticography (ECoG), or electroencephalography (EEG) – are composed of rhythmic and broadband signal information [1, 2]. This information can be quantified by estimating the power spectrum, which decomposes the variance of a signal across frequencies [3, 4, 5]. Since field potentials themselves are driven by the superposition of many underlying subprocesses [6, 7], the neural power spectrum reflects the frequency content of these subprocesses. By separating the power by frequency, the power spectrum can reveal the effects of subprocesses that have very small magnitude at high frequencies, which would be hidden in the time domain by larger low-frequency effects. A long history of empirical work has identified spectral features that reliably correlate with brain states, originally with rhythms that show up as narrowband peaks, and more recently extending to broadband features related to the shape of power spectrum across wide frequency ranges. These rhythmic and broadband spectral features are useful tools for quantifying power spectral effects, but they provide an incomplete picture of brain states and their underlying dynamics. To better understand healthy and pathological brain dynamics measured in field potentials, it is critical to connect the features of their power spectrum to underlying biophysical processes.

Rhythmic information, sometimes referred to as periodic or oscillatory activity, has received a great deal of attention at least since Berger's [8] introduction of the 'alpha' and 'beta' waves using EEG. Since then, rhythmic activity has been associated with a wide variety of behavioral mechanisms and brain states [e.g., 9, 10, 11, 12], and has been proposed as a mechanism for information gating within and across brain regions [e.g., 13, 14, 15]. Analyses on canonical narrowband frequency ranges (e.g., theta, 4-8 Hz; alpha, 8-12 Hz) are commonly used as biomarkers to track and compare changes in rhythms under particular brain states. Focusing on traditional power spectral bands for representing periodic signals is complicated, however, by rhythms that are transient [16, 17] or not strictly sinusoidal [18, 19]. Such complexities can lead to inconsistent reporting of spectral biomarker results across different subdisciplines in neuroscience [20, 21].

Studying rhythmic activity through power spectra is additionally complicated by the presence of broadband spectral effects, in which power across a wide range of frequencies varies together without a well-defined narrowband peak, distinct from any narrowband rhythmic effects in the signal and confounding measures of narrowband power [e.g., 22, 23, 24, 25, 26, 21, 27, 28]. Broadband effects are referred to by different names in the literature, often in a nonequivalent manner. These include aperiodic activity, power law scaling, $1/f$-like activity, high-gamma activity, and scale-free activity [29, 30, 31, 32, 33, 34]. Here, we use the term 'broadband' to refer to any power spectral feature or effect without a well-defined spectral peak. At least two broadband effects clearly represented in the frequency domain have been reported as consistent biomarkers of brain state: broadband height and broadband slope.

Broadband height is typically measured by the average power in the high-gamma band (80-200 Hz), due to the rarity of narrowband rhythms in this range (c.f. sharp-wave ripples, [25, 35]). High gamma power is a reliable indicator of population firing rate [36, 37, 38, 39, 40, 41, 42, 1, 43] and dendritic activity [29, 44, 45] in the absence of rhythms. The other biomarker of the underlying network activity, spectral slope, refers to the power-law exponent required to fit a $1/f^{\beta}$-like distribution to the measured power spectrum, i.e. the slope of the spectrum on a log-log plot. Broadband slope at moderate frequency ranges (e.g. 30-100 Hz) has been shown to change systematically in a host of conditions and brain states, including excitation to inhibition (E:I) balance [46, 47], age [48, 49, 50, 51, 52, 53], epilepsy [54, 55], autism [56], sleep [57], c.f. [58], schizophrenia [59], ADHD [60, 61, 62], and treatment-resistant depression [63]–among others (see table 1 in [64] for additional references across brain states).

Rhythmic and broadband features overlap in the power spectrum, can change dynamically in time, and can interact with each other. Nevertheless, there is a critical lack of theoretical models that simultaneously capture both narrowband and broadband spectral features. Traditional models of neural dynamics, whether at the single neuron, network, or population scale, typically use low-frequency time-domain dynamics and narrowband rhythmic dynamics as benchmarks for model fit, so they do not match the high frequency variance and broadband spectral shape of observed neural signals [e.g., 65]. One category of models that does address broadband effects is empirically motivated, decomposing narrowband and broadband effects using functional regression or Gaussian processes [e.g., 66, 67, 68, 69, 70]. For example, 'specparam' (formerly 'FOOOF') fits the broadband shape as log-linear with one or more knees to capture changes in the slope, and fits rhythms as bumps added to the broadband background [68]. The tool has been applied to establish spectral biomarkers across sleep, anesthesia, cognitive tasks, and clinical contexts and has undergone independent methodological study [34]. While such spectral decomposition approaches capture both narrowband and broadband effects, they are intended for descriptive analytics and they therefore do not attempt to model their biophysical generators. This limits the interpretative value of identified rhythmic and broadband components. For example, the same underlying biological processes can have both narrowband and broadband effects on the power spectrum, leading to interactions between the components that are not captured by existing parametric spectral decomposition techniques. To address this limitation, we propose a complementary approach: using forward modeling to capture how narrowband and broadband spectral effects arise from underlying biophysical generators, how they mix together in the observed power spectra, and how they interact with each other dynamically.

To capture both rhythmic and broadband effects, we will build from an existing class of models that focuses on broadband effects in the absence of rhythms. These models explain broadband effects as arising from changes in the rates of random events (modeled as point processes), which each have a characteristic waveform shape (modeled as a linear filter) [29, 32, 46]. We refer to these models as Filtered Point Processes (FPPs). The events in question can be action potentials, leading to the prediction that higher population firing rates will cause higher broadband power at particular frequencies, but they can also be other electrical events that occur with random timing. Many of the biggest contributors to neural fields are event-like in nature: in addition to action potential events, postsynaptic potentials are thought to often be the largest contributing waveform to cortical LFP recordings [e.g., 6, 71, 72], and dendritic calcium events have been shown to be detectable on the cortical surface [45, 73].

The intuition for how random event times can create broadband spectral effects is as follows. A single, perfectly sharp spike occurring once in a time series (a delta function) has power across all frequencies, i.e. it has a flat power spectrum. A series of multiple spikes at random times also has power across all frequencies, and the amount of power is proportional to the number or rate of the spikes. If we have a series of events that are not spikes but that occur at random times, for example a series of postsynaptic potentials, the spectrum will also have power at all frequencies but it will not be flat – there will be more power at lower frequencies because the smooth waveforms act like a low-pass filter. However, the height of the power spectrum at any given frequency will still be related to the rate of the events. If the rate of events increases or decreases, the whole power spectrum will shift up and down, which is a broadband effect. Furthermore, the waveform shape will determine the shape of the power spectrum, and if there are multiple event types with different waveform shapes, their superposition can lead to complex shape and slope effects in the overall power spectrum. While this perspective can capture broadband shape effects, previous work has not attempted to additionally capture rhythmic or low-frequency effects arising from dynamics in the event rates.

Here, we generalize the original filtered point process models [e.g., 29, 32, 74] to account for a wider array of rhythmic and broadband power spectral effects. We build on previous literature in at least four ways. First, we model rhythmic or time-varying firing rates. Second, we allow for the presence of multiple interacting subprocesses, for example excitatory and inhibitory populations with dynamic coupling. Third, we derive the theoretical power spectra for the models at both long and short timescales. Finally, we show how the resulting forward modeling framework can predict important qualitative effects in neural power spectra, including transition points between rhythmically-dominated vs broadband-dominated regions of the power spectrum, and cross-frequency coupling at sub-second timescales. By relating proposed biophysical subprocesses to their dynamic narrowband and broadband effects on the power spectrum, our framework will enable practitioners to test candidate models of the biophysical sources of changes in spectral shape and cross-frequency coupling.

## Theory

Filtered point process models start from the idea that the biophysical generators of neural voltage recordings are mostly characterized by discrete events, such as local action potentials, postsynaptic potentials, and dendritic spiking events [6, 7]. In other words, continuous neural signals are generated by processes that may be modeled as point processes. The event-like nature of the processes underlying the recordings is not always clear because each event is not a perfect spike, but rather has a characteristic temporal shape or waveform: if the rate of events is very high, the contribution of each event will be obscured in the time domain. Nevertheless, the event rates and the shapes of their waveforms will have predictable consequences on the power spectrum of the signal.

FPP models take the perspective of a recording electrode in space, modeling the field potential as the superposition of the voltage response generated by subprocesses representing several different event types. Figure 1 shows an example of this approach, describing how the shape of the power spectrum of surface ECoG recordings in macaques changes under propofol anesthesia (data from [75], model extended from [46]. See Supplemental Material for details). The observed power spectrum (Panel A) changes dramatically from the awake state to the unconscious state. We model the signal as a superposition of two subprocesses (Panel B), related to the excitatory synapses (red) and inhibitory synapses (blue) on the pyramidal cells underlying the electrode. Each subprocess is modeled as a random time series of postsynaptic events, filtered by the characteristic postsynaptic current shape (Panel B, insets). By formally modeling this structure, we can derive the theoretical power spectrum of the combined model (Panel C). Each subprocess contributes two components to the power spectrum: one component related to the time-varying rhythms or ensemble dynamics (solid red/blue lines) and one component related to the broadband effects of random event times (dashed red/blue lines). The theoretical power spectrum of the model (black line) is a combination of these components.

The example in Figure 1 Panel C illustrates how models of this form can be used to test the ability of proposed mechanisms to explain power spectra and support hypothesis generation. In the awake state, the LFP spectrum across all frequencies is well described by postsynaptic potentials [6], with an AMPA-GABA mediated alpha rhythm [8, 76, 77]

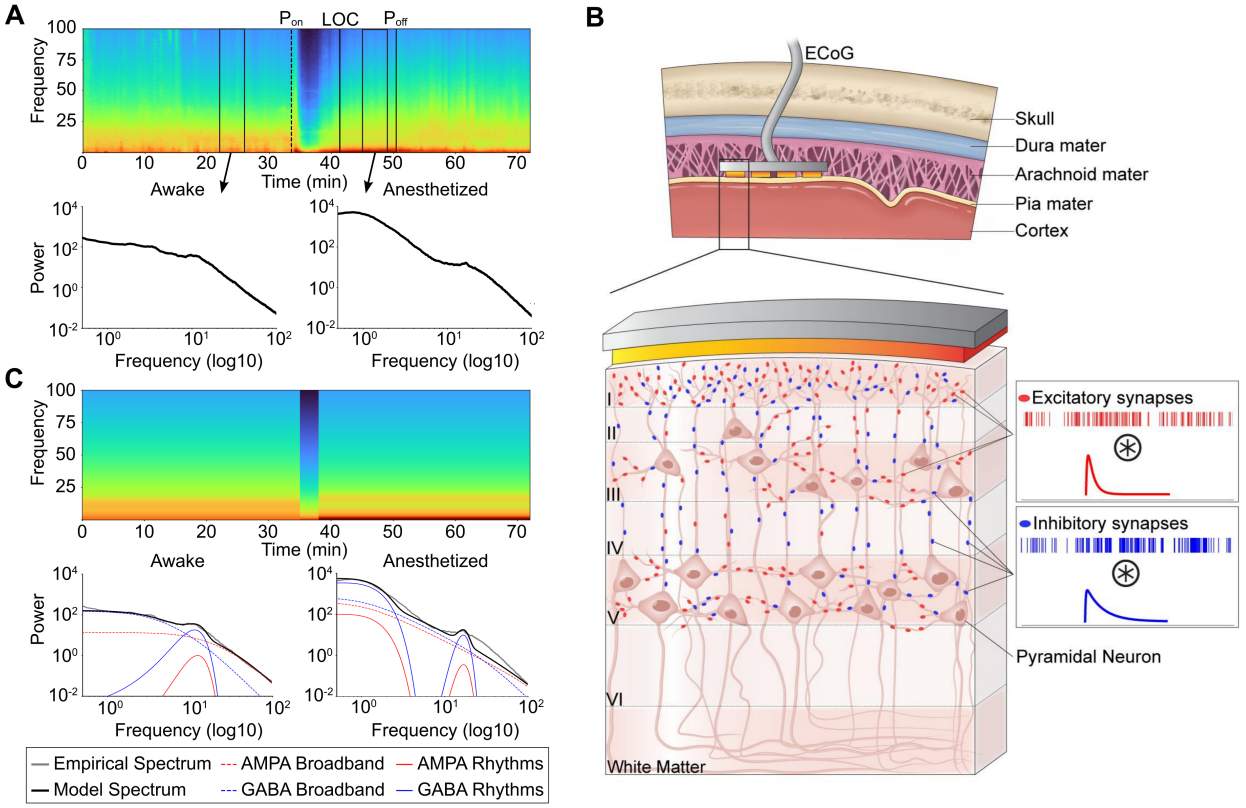


Figure 1: **Filtered point process models describe field recordings as a superposition of event type subprocesses.** Shown is a motivating use case for the filtered point process (FPP) framework: modeling the influence of excitatory and inhibitory synaptic dynamics on surface voltage recordings. (A) Spectrotemporal analysis of electrocorticography (ECoG) recordings from a monkey undergoing propofol anesthesia using data from [75]. (Above) Spectrogram of the entire session ($P_{on}$: propofol onset; $LOC$: loss of behavioral consciousness; $P_{off}$: propofol offset) (Below) Mean power spectra from the Awake and Anesthetized (behaviorally unconscious) states. (B) FPPs model multiple subprocesses; here, excitatory (red) and inhibitory (blue) synaptic events on the pyramidal cells underneath the electrode. Each subprocess has a stereotyped waveform occurring at random event times (insets). (C) Example FPP models of the awake and anesthetized states shown in Panel A. The models allow a decomposition of the power spectra into rhythmic (solid lines) and broadband (dashed lines) components. See Supplemental Material for data and modeling details.

and with inhibitory activity dominating low frequencies [7]. In the unconscious state under propofol, classic theory would include a slow wave and an alpha rhythm [76, 78, 79, 80, 77], with a steeper spectral slope at high frequencies due to increased inhibition [46]. When we include just those elements in this model, it fails to describe the power between $\sim$ 30 and 100 Hz. This could motivate us to iteratively adjust the model, for example with a beta-gamma rhythm [81] or with alternative broadband effects [82, 83, 28]. Below, we will describe previous work with related models and then present the details of our modeling framework.

### Related work: Filtered homogeneous Poisson process modeling

Filtered homogeneous Poisson point processes [FHPP; e.g., 84] are a special instance of the more general FPP framework in which the event rates do not change in time. FHPPs have emerged as an approach for modeling both temporal and spectral information in field potentials in the absence of narrowband oscillations [e.g., 29, 32, 74, 85, 46, 86, 87, 28], and they illustrate how FPPs can be used in both theoretical and applied neuroscience research. In FHPPs, each subprocess only contributes a broadband component to the total power spectrum, and the overall spectral shape reflects the relative firing rates of the subprocesses. FHPPs have been used to justify the relationship between population firing rates and the broadband height of the power spectrum [24, 1, 23, 25, 35, 85], as well as how excitatory-inhibitory balance can influence the slope of the power spectrum [46]. These theoretical studies used forward modeling and simulation to postulate the generators of observed effects, and they have motivated applied research, such as in brain-computer

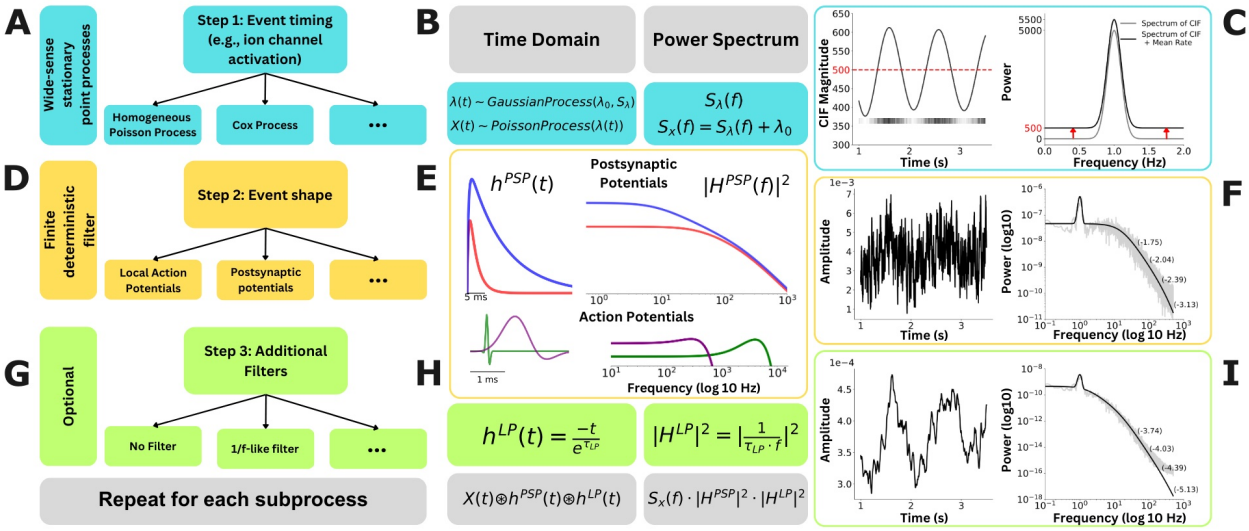


Figure 2: **The filtered point process (FPP) framework. (Row 1: A-C) Event time series with optionally dynamic rates** (A) A wide variety of point processes can be integrated into the FPP framework provided that the point process itself is wide-sense stationary. (B) One desirable example is the Cox process, a point process with a random CIF, here modeled by a spectrally-defined Gaussian Process. (C) (Right) The theoretical spectrum of an example CIF (gray) with peak power at 1 Hz and a peak width of 0.1 Hz; the point process spectrum (black) is shifted up by 500 (the mean rate) on a linear scale. (Left) A realization of the CIF, with mean 500 $spikes/sec$. The raster plot below shows the point process event times. **(Row 2: D-F) Event waveform filters** (D) Any linear, finite, and deterministic filter can be used in the FPP. (E) Several filter templates have been derived. Top: two postsynaptic potentials $h^{PSP}(t)$, AMPA (red) and GABA (blue), defined in the time domain, and $H^{PSP}(f)$, capturing the effects of the filters on the power spectrum. Bottom: two action potentials (AP), regular spiking (green) and fast spiking (purple). (F) The effect of a GABA filter on the point process example from Panel C: (Left) the effect on the time-domain realization; and (Right) the effect on the theoretical (black) and empirical (gray) power spectra. Slopes of the theoretical power spectrum at four points are annotated in parentheses. **(Row 3:G-I) Optional additional filters** (G) Additional filters can be used to capture different shape effects driven by the system being modeled. (H) (Left) A generic low-pass filter specified in the time domain, and (Right) its effect on the power spectrum in the frequency domain. Below in gray is the theoretical solution for the full model in the time and frequency domain. (I) Results of the final model for the local field potential (Left) in the time domain and (Right) the theoretical (black) and empirical (grey) power spectra of the process, with four example slopes annotated in parentheses.

interfaces [36, 37, 38, 39, 88], where high gamma power (80-200 Hz) is a common proxy for population firing rates. The success of these models in both theoretical and empirical research speaks to their substantial explanatory power, despite the simplicity (and linearity) of their structure.

Despite the value of the FHPP models, they do not allow for narrowband effects like rhythms, because they assume a constant firing rate. However, trial-based experiments and many brain states have complex firing rates and oscillations that vary as a function of time. Further, prior models have not accounted for multiple interacting subprocesses, which would be necessary to model coherent rhythms. By generalizing FPPs to allow time-varying and coherent firing rates, we extend their explanatory power by capturing more features of observed power spectra.

## Model Structure

The FPP framework has a modular structure (Figure 2), building up a model based on the (1) event timing and (2) event waveforms for the subprocesses of interest, with (3) the option to add additional filters to capture effects such as low-pass filtering due to properties of the extracellular medium. A given subprocess represents the information from many different sources (e.g., synapses) from many different neurons in the vicinity of the electrode. In the next few sections, we will build up a model example using Figure 2, where Panels C, F, and I show the time and frequency representations of an example model.

## Event Timing

The basis of the model are a set of event types in the neural tissue underlying the electrode, such as postsynaptic potentials, which are considered to be important contributors to the rhythms and/or broadband power in the spectrum. The event *times* are modeled by point processes (Figure 2, teal), capturing the structure of the randomness in the event times [89]. In general, point processes are parameterized by a Conditional Intensity Function (CIF) $\lambda(t)$, which captures the instantaneous rate of events; note that any point process can be fully specified by its CIF, which is given as the joint probability density of event times [89]. For example, homogeneous Poisson processes assume that the CIF is constant in time $\lambda(t) = \bar{\lambda}$. By allowing the CIF to vary randomly in time, we can account for dynamic variation in the mean-field or ensemble dynamics of the event type. This is achieved by a Cox process, a point process where the CIF is itself a stochastic process [84, 89, 90, 91], making the overall point process "doubly stochastic" (i.e. the CIF is random and the event times are random conditioned on the CIF).

Figure 2 Panels B and C show an example of a Cox process that can capture a slow oscillation at 1 Hz (details in Methods). The time-varying CIF is modeled by a Gaussian process with mean $\lambda_0$ and power spectrum $S_\lambda(f)$, where the power spectrum contains a narrowband peak at 1 Hz (Panel C, gray line). The point process is then modeled as an inhomogeneous (i.e. time-varying) Poisson process where the rate $\lambda(t)$ is the realization of the Gaussian process:

$$\lambda(t) \sim GaussianProcess(\lambda_0, S_\lambda(f)) \tag{1}$$

$$X(t)|\lambda(t) \sim PoissonProcess(\lambda(t)) \tag{2}$$

where $X(t)$ is a time series representing the random event times of the Poisson process. Here we assume that the mean rate $\lambda_0$ is large enough that the fluctuations in the CIF $\lambda(t)$ are highly unlikely to be negative. This assumption is often justified by the large number of event generators (e.g. synapses, cells) in the vicinity of a recording electrode. In cases where the assumption is unlikely to hold, a link function can be used to guarantee non-negative event rates, such as a log link function [5].

We can also represent $X(t)$ by its counting process, $N_k$, which represents the number of spikes in discrete bins, where bin $k$ is defined as the interval from time $k\Delta t$ and time $(k+1)\Delta t$. The number of events in any time bin is Poisson distributed, and the rate is approximated by the CIF at time $k\Delta t$:

$$N_k \sim Poisson(\lambda(k\Delta t)\Delta t) \tag{3}$$

for small $\Delta t$. In neuroscience recordings, it is common to choose $\Delta t = 1ms$, and represent $N_k$ as a 0-1 vector in discrete time. The framework is flexible with regard to discrete and continuous representations of time.

By definition, the power spectrum of a stochastic process is the Fourier transform of the autocovariance function (dependence across time lags) of the process, so it fully describes the second moment of the process in the frequency domain [3, 4, 5]. Spectral analysis assumes that the process is weak-sense stationary, meaning that the first moment (mean) and second moment (autocovariance) do not vary in time within the time window that is being analyzed. Here, because the time-varying $\lambda(t)$ is governed by a stationary Gaussian process, the overall point process is also stationary. Hence, the process (and by extension the full FPP model) has a well-defined power spectrum.

We would like to understand the structure of the power spectrum of the point process $X(t)$, since it will form the basis of the power spectrum of the full filtered point process. A technical detail here is that point processes use a generalized notion of a power spectrum, the Bartlett spectrum. For our purposes, it is sufficient to know that the Bartlett spectrum behaves like a standard spectrum under filtering [90]. The Bartlett spectrum of $X(t)$ contains two terms, one related to the power spectrum of the CIF and one related to the mean rate [92, 90]:

$$S_X(f) = S_\lambda(f) + \lambda_0 \tag{4}$$

The mean rate of events ($\lambda_0$) controls the height of the spectrum at all frequencies. Temporal dependence in the CIF (rhythms, autocovariance) will lead to variations in the spectrum across frequencies ($S_\lambda(f)$).

Figure 2 Panel C shows how this works for the slow wave Cox process example: on the left, a realization of the process has a CIF (solid black line) that oscillates at approximately 1 cycle per second and an event timeseries (black raster plot) where events are more likely to occur when the CIF is high than when it is low. On the right, the theoretical power spectrum of the Cox process (black line) is the sum of the power spectrum of the Gaussian process (gray line) and a flat component equal to the mean rate (here 500 $spikes/sec$). We will refer to this flat component as the "broadband" component of the power spectrum.

## Event Shape

Each point process is filtered with an event shape or waveform, which corresponds to the extracellular waveform of the biological process of the corresponding event type (Figure 2, yellow). These can range from action potentials, which

may account for as much as 20% of the electrical field [72], to postsynaptic potentials, which are thought to make up the bulk of local field potentials [93, 6, 7]. Waveforms can be flexibly defined, and their effect on the theoretical power spectrum is analytically tractable whenever the Fourier transform is well-defined. We refer to the time domain representation of events as "waveform," "filter," or "event shape," whereas a "kernel" is the magnitude squared of the Fourier transform of the waveform. The filter information can be combined with point process information in the time and frequency domains through a convolution in the time domain or multiplication in the frequency domain, retaining the tractability of the solution.

Figure 2 Panel E shows four example waveforms: two postsynaptic potential types (AMPA and GABA, in red and blue), and two action potential types (regular spiking and fast spiking, in green and purple; see Methods for details).

For postsynaptic potentials, we use the difference of two exponentials as a generic functional form, which can be tuned by its rise and decay time constants to capture the dynamics of different channel types [46, 71, 86, 94]. Let $h^{PSP}(t)$ be the shape of the postsynaptic potential in the time domain:

$$h^{PSP}(t) = e^{\frac{-t}{(\tau_{\text{rise}})}} + e^{\frac{-t}{(\tau_{\text{decay}})}} \tag{5}$$

where $\tau_{\text{rise}}$ and $\tau_{\text{decay}}$ are the rise and decay time constants of the postsynaptic currents, which will vary depending on the type of synapses (i.e., AMPA and GABA synapses).

For the action potential waveforms, we use a real Gabor function (c.f. [86]), which can be tuned to create fast and slow action potentials:

$$h(t) = k \cdot \exp\left(-\frac{(t-t_0)^2}{2\sigma^2}\right) \cdot \cos\left(2\pi f_0(t-t_0) + \theta\right) \tag{6}$$

where $k$ is the amplitude of the action potential, $f_0$ is the center frequency of the cosine function, and $\theta$ is the phase offset.

For any event type, the filter $h(t)$ is applied to the point process $X(t)$ in the time domain via a convolution:

$$Y(t) = X(t) \circledast h(t) = \sum_n h(t - t_n) \tag{7}$$

where $t_n$ are the times of the events in $X(t)$.

This convolution in the time domain will correspond to a multiplication in the frequency domain (i.e., a Fourier pair). If we let $\mathcal{H}(f)$ be the Fourier transform of $h(t)$, then the effect of the filter will be to multiply the power spectrum of $X$, $S_X(f)$, by the magnitude squared of $\mathcal{H}$ [3]:

$$\begin{aligned} S_Y(f) &= |\mathcal{H}(f)|^2 S_X(f) \\ &= |\mathcal{H}(f)|^2 S_\lambda(f) + |\mathcal{H}(f)|^2 \lambda_0 \end{aligned} \tag{8}$$

Notice that the overall power spectrum decomposes into two terms, inherited from the two terms in Equation 4: the first term relates to the dynamics of the event rates, and the second term relates only to the mean rate of the events. While both terms are shaped by the frequency-dependence of the filter, the first term will typically be narrowband, while the second term will typically be broadband. Equations 7 and 8 hold for any wide-sense stationary point process and finite, deterministic filter selection.

The waveforms in Panel E have well-defined Fourier transforms, which can be used to compute the kernel $|\mathcal{H}(f)|^2$ and applied to Equation 8 to derive the theoretical power spectrum of the FPP. For the postsynaptic potentials (Equation 5), the Fourier transform is:

$$\mathcal{H}^{PSP}(f) = \frac{1}{\frac{1}{\tau_{\text{decay}}} + i2\pi f} - \frac{1}{\frac{1}{\tau_{\text{rise}}} + i2\pi f} \tag{9}$$

And for the action potentials (Equation 6), the Fourier transform is:

$$\mathcal{H}(f) = k \cdot k_2 \left[\exp\left(-\frac{\sigma^2}{2}\left(\omega + 2\pi f_0\right)^2 - i\left(\theta + t_0\omega\right)\right) + \exp\left(-\frac{\sigma^2}{2}\left(\omega - 2\pi f_0\right)^2 + i\left(\theta - t_0\omega\right)\right)\right] \tag{10}$$

where $\omega = 2\pi f$ is the angular frequency and $k_2$ is a distinct scaling constant (see Supplement 4 for full equation).

The framework can also be used in conjunction with empirically fit waveforms, such as action potential shapes that are known to vary across cell types [95, 96, 97, 98, 99, 100]; in this case, a discrete Fourier transform can be used to compute the kernel of the empirical waveform.

Figure 2 Panel F shows the effects of applying a GABA waveform to the time-domain realization and theoretical power spectrum of the Cox process from Panel C. In the time domain realization (left), the waveform transforms the time series from a sequence of events into a noisy continuous-time signal, where the 1 Hz rhythmic structure in the event rates is visible in the trend. In the power spectrum (right), the spectral peak from the CIF is still present, and the broadband component has been shaped by the function $|\mathcal{H}^{PSP}(f)|^2$, which is approximately flat for low frequencies and curves down with a noticeable negative slope above 10 Hz. In fact, for the postsynaptic potential shape shown in Figure 2 Panel E and used in the model for Panel F, the slope of the filter will converge to $\beta = -4$ in log-log space as frequency tends to infinity (see Supplemental Materials for derivation). However, as shown in Figure 2 Panel F, this limiting slope does not apply to these models until frequencies above those typically examined in neuroscience studies.

## Additional Filters

While the properties of event timing and waveform shape play a large role in the shape of the power spectrum on an extracellular electrode, there may be other effects that need to be modeled using additional filters – either for theoretical reasons or to achieve a better match to empirically observed data.

For example, additional filters could capture the transformation of transmembrane currents to extracellular potentials, based on the biophysical properties of the cell membrane and extracellular medium [101, 93, 71, 102]. The underlying properties of extracellular media and their effect on the frequency scaling of field potentials continue to be an active area of research. As such, we include this unknown in our modeling framework by including the possibility of additional filters that can be designed to represent the desired biophysical effects.

Additional filters can also be helpful to match empirically observed data. An empirical effect that has been of particular interest because of its ubiquity across spatial scales and recording modalities is the power-law scaling property of field potential power spectra. “Power-law scaling" or “$1/f^{\beta}$ frequency scaling" refers to the empirical observation that the power spectrum often forms a line in some frequency ranges when plotted on log-log axes, i.e. the power in log space is inversely proportional to the frequency $f$ increased to an exponent $\beta$ [103, 32, 64]. The exponent $\beta$ is referred to as the “spectral exponent" or “spectral slope", and empirical spectral exponents of neural power spectra vary between about -2.5 and -4 across a variety of healthy and diseased brain states [64]. As shown in Figure 2 Panel F, an FPP model with only a postsynaptic potential filter has slopes between zero and -3.1 for frequencies below 1000 Hz. Additional theoretically justified low-pass filters may be helpful to capture steeper slopes.

For example, a simple low-pass filter representing the effects of ionic diffusion can be given as:

$$h^{LP}(t) = e^{\frac{-t}{\tau_{LP}}} \tag{11}$$

where $\tau_{LP}$ is the time constants of the filter. The Fourier transform of the filter is:

$$\mathcal{H}^{LP}(f) = \frac{1}{\tau_{LP} \cdot f} \tag{12}$$

When applied to the model with postsynaptic potentials (Equations 7), the filter operates as a convolution in the time domain:

$$Y^{LP}(t) \quad = \quad X(t) \circledast h^{PSP}(t) \circledast h^{LP}(t) \tag{13}$$

and the power spectrum (Equation 8) is shaped by the filter kernel:

$$S_Y^{LP}(f) \quad = \quad |\mathcal{H}^{LP}(f)|^2 |\mathcal{H}^{PSP}(f)|^2 S_X(f) \tag{14}$$

Figure 2 Panel I shows the impact of this low-pass filter on the signal from Panel F. In the time-domain realization (left), the filter smooths out much of the noise in the signal, and the 1 Hz oscillation is more apparent. In the power spectrum (right), the filter has tilted the entire power spectrum, making the slopes more negative, although the original 1 Hz spectral peak is still visible. Here, the the low-pass filter itself has a spectral slope of $\beta = -2$ and, when combined with the spectrum in Panel I, the whole model will have a limiting slope of $\beta = -6$ (see Supplemental Materials for derivation). Ultimately, the final power spectrum captures both periodic information, through the dynamics of the CIF, and broadband information, through the stochastic point process.

## FPPs can model multiple subprocesses simultaneously

When multiple subprocesses are modeled, for example both AMPA and GABA postsynaptic potentials, the field recording is considered to be the superposition or sum of the filtered subprocesses:

$$Y^{field} = \sum_j Y^j \tag{15}$$

where $Y^j$ are the filtered subprocesses, for example described by Equation 13.

In this case, it is important to model the dynamic dependence of the subprocesses, because coherence between subprocesses will affect power spectrum of the field recording. For example, if we have two point processes relating to AMPA and GABA postsynaptic potentials, we can model their CIFs using a bivariate Gaussian process, and the point processes as a bivariate Poisson process conditioned on the rates from the Gaussian process:

$$\begin{aligned} \begin{bmatrix} \lambda^A(t) \\ \lambda^G(t) \end{bmatrix} &\sim BivGaussProc\left(\begin{bmatrix} \lambda_0^A \\ \lambda_0^G \end{bmatrix}, C_{\lambda,AG}(f)\right) \\ \begin{bmatrix} X^A(t) \\ X^G(t) \end{bmatrix} &\sim BivPoissProc\left(\begin{bmatrix} \lambda^A(t) \\ \lambda^G(t) \end{bmatrix}\right) \end{aligned} \tag{16}$$

where $A$ refers to the AMPA subprocess, $G$ refers to the GABA subprocess, and $\lambda_0$'s are the overall mean rates. For each frequency $f$, $C_{\lambda,AG}(f)$ is a $2 \times 2$ cross-spectral matrix of the CIFs, which can be written as:

$$C_{\lambda,AG}(f) = \begin{bmatrix} S_{\lambda,A}(f) & S_{\lambda,AG}(f) \\ S_{\lambda,AG}(f)^* & S_{\lambda,G}(f) \end{bmatrix} \tag{17}$$

where $S_{\lambda,A}(f)$ and $S_{\lambda,G}(f)$ are the power spectra of the AMPA and GABA CIFs at frequency $f$, respectively, and $S_{\lambda,AG}(f)$ is the scalar cross-spectrum (the Fourier transform of the cross-covariance function) between the two CIFs at frequency $f$. This captures the coherence structure between the two CIFs, because (complex) coherence is defined as the normalized cross-spectrum:

$$\frac{S_{\lambda,AG}(f)}{\sqrt{S_{\lambda,A}(f)S_{\lambda,G}(f)}} \tag{18}$$

We assume that the only dependence between the processes is via the CIFs, i.e. that the actual event times are conditionally independent after accounting for the CIFs. If the two CIFs are independent, then $S_{\lambda,AG}(f) = 0$ for all frequencies.

Understanding the effect of dependence between subprocesses on the FPP model amounts to describing how each model choice affects the cross-spectrum of the resulting process. First, the cross-spectrum of the bivariate point process is given by [89]:

$$\begin{aligned} C_{X,AG}(f) &= \begin{bmatrix} S_{X,A}(f) & S_{X,AG}(f) \\ S_{X,AG}(f)^* & S_{X,G}(f) \end{bmatrix} \\ &= \begin{bmatrix} S_{\lambda,A}(f) + \lambda_0^A & S_{\lambda,AG}(f) \\ S_{\lambda,AG}(f)^* & S_{\lambda,G}(f) + \lambda_0^G \end{bmatrix} \end{aligned} \tag{19}$$

We can see from these equations that the mean rates $\lambda_0^A$ and $\lambda_0^G$ only affect the diagonal terms (the power spectra), not the dependence between the two processes (the cross-spectrum).

Applying filters to the model will shape both the spectra and the cross-spectrum. For example, if we filter $X^A(t)$ by $h^A(t)$, the AMPA waveform, and $X^G(t)$ by $h^G(t)$, the GABA waveform:

$$\begin{bmatrix} Y^A(t) \\ Y^G(t) \end{bmatrix} = \begin{bmatrix} X^A(t) \\ X^G(t) \end{bmatrix} \circledast \begin{bmatrix} h^A(t) \\ h^G(t) \end{bmatrix} \tag{20}$$

then the cross-spectral matrix will be (suppressing the dependence on $f$ for compactness)[3]:

$$C_{Y,AG} = \begin{bmatrix} |\mathcal{H}^A|^2 S_{X,A} & \mathcal{H}^A \mathcal{H}^{G*} S_{X,AG} \\ \mathcal{H}^G \mathcal{H}^{A*} S_{X,AG}^* & |\mathcal{H}^G|^2 S_{X,G} \end{bmatrix} \tag{21}$$

where, as before, $\mathcal{H}^A(f)$ and $\mathcal{H}^G(f)$ are the Fourier transforms of $h^A(t)$ and $h^G(t)$, respectively. We can see that the spectra on the diagonals are transformed as expected from Equation 8, and the cross-spectrum is shaped by the product of the kernels or the Fourier transforms of the AMPA and GABA waveforms. This step can be repeated for any additional desired filters.

Finally, the power spectrum of the final field recording $Y^{field}$, as defined in Equation 15 will be:

$$S_{field} = \sum_j \sum_k S_{Y_j,Y_k} \tag{22}$$

or in the AMPA and GABA example:

$$\begin{aligned} S_{field} &= |\mathcal{H}^A|^2 S_{X,A} \\ &\quad + \mathcal{H}^A \mathcal{H}^{G*} S_{X,AG} \\ &\quad + \mathcal{H}^G \mathcal{H}^{A*} S^*_{X,AG} \\ &\quad + |\mathcal{H}^G|^2 S_{X,G} \end{aligned} \tag{23}$$

Additional filters that are applied equally to all components represented in $S_{field}$, such as the low pass filter $|\mathcal{H}^{LP}(f)|^2$ introduced in Equation 14, can simply be represented as:

$$S^{LP}_{field} = |\mathcal{H}^{LP}(f)|^2 S_{field} \tag{24}$$

This would then be distributed as

$$\begin{aligned} S^{LP}_{field} &= |\mathcal{H}^{LP}(f)|^2 |\mathcal{H}^A|^2 S_{X,A} \\ &\quad + |\mathcal{H}^{LP}(f)|^2 \mathcal{H}^A \mathcal{H}^{G*} S_{X,AG} \\ &\quad + |\mathcal{H}^{LP}(f)|^2 \mathcal{H}^G \mathcal{H}^{A*} S^*_{X,AG} \\ &\quad + |\mathcal{H}^{LP}(f)|^2 |\mathcal{H}^G|^2 S_{X,G} \end{aligned} \tag{25}$$

We now present two special cases of this bivariate FPP structure with AMPA and GABA synapses: independent subprocesses and processes that share a CIF up to a linear transform.

First, if the processes (including their CIFs) are independent, then the off-diagonal elements of the cross-spectral matrix (Equation 17) are zero for all frequencies, so the final field spectrum will simply be the sum of the spectra of the two processes:

$$\begin{aligned} S_{field} &= |\mathcal{H}^A|^2 S_{X,A} + |\mathcal{H}^G|^2 S_{X,G} \\ &= |\mathcal{H}^A|^2 S_{\lambda,A} + \mathcal{H}^A|^2 \lambda^A_0 \\ &\quad + \mathcal{H}^G|^2 S_{\lambda,G} + |\mathcal{H}^G|^2 \lambda^G_0 \\ &\quad \text{[Independent]} \end{aligned} \tag{26}$$

If the processes share a CIF up to a linear transform, i.e. if:

$$\begin{bmatrix} \lambda^A(t) \\ \lambda^G(t) \end{bmatrix} = \lambda(t) \begin{bmatrix} w_A \\ w_G \end{bmatrix} + \begin{bmatrix} \lambda^A_0 \\ \lambda^G_0 \end{bmatrix} \tag{27}$$

where $\lambda(t)$ is a univariate Gaussian process with spectrum $S_\lambda(f)$ and $w_A$, $w_G$, $\lambda^A_0$, $\lambda^G_0$ are known parameters, then the power spectrum of the CIF will have a term for the spectrum of the CIF, shaped by the two kernels, and two terms related to the mean rates of the processes:

$$\begin{aligned} S_{field} &= \kappa S_\lambda + |\mathcal{H}^A|^2 \lambda^A_0 + |\mathcal{H}^G|^2 \lambda^G_0 \\ \kappa(f) &= w_A^2 |\mathcal{H}^A|^2 + w_A w_G^* \mathcal{H}^A \mathcal{H}^{G*} \\ &\quad + w_A^* w_G \mathcal{H}^G \mathcal{H}^{A*} + w_G^2 |\mathcal{H}^G|^2 \\ &\quad \text{[Linearly Dependent]} \end{aligned} \tag{28}$$

Hence, as in the case with only one subprocess (Equation 8), the power spectrum for a model with multiple subprocesses decomposes into terms related to the spectra of the CIFs (typically narrowband) and terms related to the mean rates (typically broadband).

## Results

### Result 1: FPP power spectra are dominated by either ensemble dynamics or broadband at different frequencies

Power spectral effects in neural voltage recordings tend to show frequency ranges that are dominated by either rhythmic or broadband effects — this is the basis for defining canonical rhythms (e.g. slow <1 Hz) and fixed bands for broadband

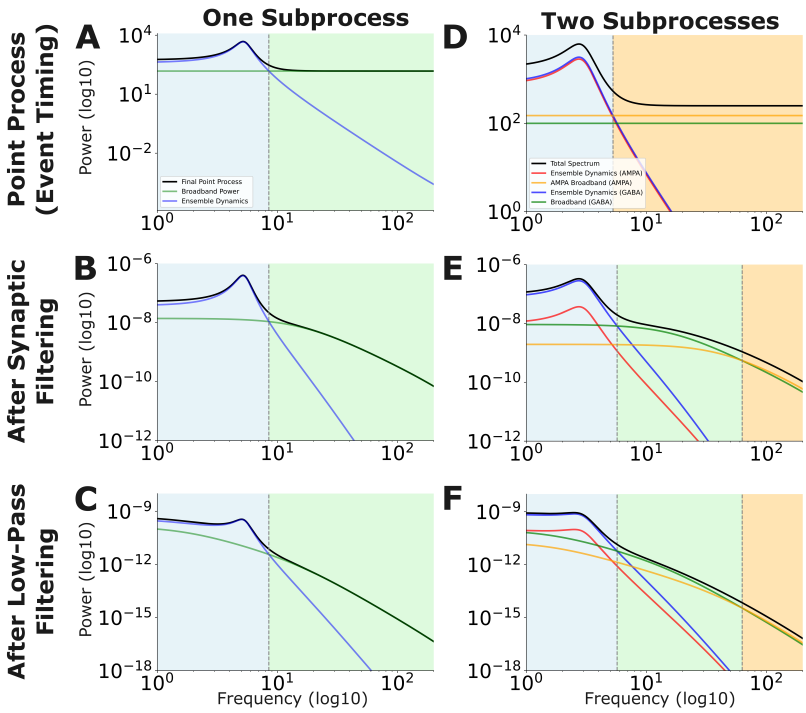


Figure 3: **Filtered point process (FPP) models exhibit transition points in their spectra.** *Column 1*: A GABA subprocess is modeled as a Cox process with an AR(2) CIF (blue line) and a mean rate (green). The overall theoretical spectrum for each modeling step is given in black. (A) The mean rate component and the spectrum of the conditional intensity function (CIF) produces a transition point $\sim$ 7.3 Hz. This produces two regions of the power spectrum, CIF-dominated (blue shading) and broadband-dominated (green shading) region. Applying the GABA filter (B) and a 1/f-like low-pass filter (C) changes spectral shape but does not change the transition point. *Column 2*: Two independent AMPA and GABA subprocesses are modeled, each with AR(2) CIFs. The overall theoretical spectrum for each modeling step is given in black. (D) The CIFs of the AMPA and GABA process (unfiltered) are shown in orange and blue, respectively, and their broadband components are in red and green. Shading reflects the dominant component, as before, and the transition point is $\sim$ 5.27 Hz. (E) Filtering the subprocesses by different filters (the AMPA and GABA event shapes) changes the transition points. The final spectrum now has two transition points: GABA ensemble dynamics dominate below $\sim$ 5.7 Hz, GABA broadband dominates from 5.7-62.65 Hz, and AMPA broadband dominates above 62.65 Hz. E) Spectra after applying a 1/f filter: the transition points do not change.

power (e.g. high gamma 80-200 Hz). Empirically, rhythms tend to dominate at lower frequencies and broadband effects tend to dominate at higher frequencies. Rhythmic or not, the lower frequencies can be dominated by coherent afferent projections to the recorded area [e.g., 104, 105, 106]. Signals traveling longer distances tend to exhibit slower temporal dynamics, which lend themselves well to synchronization (e.g., [107]). In contrast, higher frequency components are correlated with local firing behavior, as described above [108, 105, 32, 42, 109]. FPP models capture and explain this property of neural power spectra: frequencies will either be dominated by “ensemble dynamics", i.e. the power spectrum of the rate process (CIF), or “broadband", i.e. the flat power spectrum arising from random event times. This is a direct result of the power spectrum of a point process given in Equation 4.

In Figure 3, we demonstrate this effect using a FPP model with a single GABA subprocess for simplicity. The mean rate $\lambda_0$ and the spectrum of the CIF $S_\lambda(f)$ are shown in Figure 3 Panel A, green and blue lines, respectively. The mean rate component is “broadband” because it has constant power across all frequencies. If the modeled point process is a homogeneous Poisson process, this broadband component is the only spectral information present. When a FPP is modeled using a Cox process, its power spectrum is additionally affected by the power spectrum of the CIF. We refer to this component as the “ensemble dynamics" in a neuroscience context because it describes the temporal structure of the rate process for the event type, e.g. the dynamic rate averaged across all GABA synapses in the ensemble. In Figure 3, the CIF is modeled as an AR(2) process that has a spectral peak.

For any single subprocess modeled as a Cox FPP, both the ensemble dynamics and broadband information have the potential to contribute at any frequency. However, FPP models predict that certain components of the model will

dominate at certain frequencies, leading to overall power spectral shape effects. Figure 3 Panel A shows the power spectrum of a point process with an AR(2) CIF. The overall power (black line) at frequencies shaded in blue primarily reflects information contributed by the ensemble dynamics (blue line) and the power at frequencies shaded in green primarily reflects information contributed by the broadband (green line). Around 7.3 Hz, there is a transition point: ensemble dynamics power dominates below 7.3 Hz and the broadband power dominates above 7.3 Hz. This pattern of different components dominating at different frequencies has been observed before in other filter-based models [110, 28]. Given the parameters of the ensemble dynamics, there will be a transition point as long as the mean rate line crosses the CIF line.

Importantly, the location of the transition point does not change when the process is filtered: Figure 3 Panel B shows the power spectrum after applying the GABA postsynaptic potential shape to each event via filtering, and Panel C applies an additional 1/f-like filter. It can be seen that the transition point is identical after filtering, i.e. any given frequency is dominated by either ensemble dynamics or broadband power, and the choice is determined at the level of the point process, regardless of any subsequent filtering.

This has several practical implications for interpreting empirical neural power spectra. First, according to this model, rhythmic effects and broadband effects are not additive in log space, as some spectral decomposition methods assume [68, 111]. Rather, the effects are additive in linear space [112, 66, 70], causing the largest component to dominate when viewed on a log scale. Second, broadband shape effects such as the spectral slope or power law exponent will be effectively invisible at frequencies that are dominated by rhythms or other ensemble dynamics. To estimate the spectral slope it is therefore necessary to restrict analysis to frequencies that are dominated by broadband effects. Note that in some cases, the power law exponent of the ensemble dynamics may be of interest [113, 49, 114, 115, 116] in which case it will be important to restrict analysis to frequency ranges dominated by those effects.

**Result 2: Multiple FPP subprocesses can produce complex spectral shape effects explained by simple model components**

Parsimonious descriptions of field potentials will typically highlight at least two subproccesses as the primary drivers of a neural recording. FPPs can accommodate this by modeling multiple subprocesses with either independent or dependent temporal structure. Here, we focus on two independent subprocesses, process 1 (ultimately filtered by an AMPA waveform) and process 2 (ultimately filtered by a GABA waveform), and show that the components of the subprocess power spectra themselves have transition points that can be useful in explaining complex power spectral shape effects.

Figure 3 Panel D shows two independent point processes modeled with nearly identical ensemble dynamics modeled as AR(2) processes (process 1 in orange and process 2 in blue). Additionally, process 1 and process 2 have two different broadband components, shown in red and green respectively. As with the previous section, each subprocess has one transition point between the ensemble dynamics and broadband. Overall, lower frequencies are dominated by the process 2 ensemble dynamics and the higher frequencies are dominated by process 1 broadband, so the highlighted transition point is between two different subprocesses.

When introducing the AMPA (process 1) and GABA (process 2) filters in Panel E, more complex relationships arise. First, as expected, the transition point within each subprocess is preserved (green/blue crossing and red/orange crossing). However, there is a change in the overall dominant component from applying different filters to each subprocess. While the GABA ensemble dynamics still dominate at low frequencies (blue shading in Figure 3), in this model the addition of the postsynaptic filters allows the GABA and AMPA broadband components to cross and create a region where GABA broadband dominates (shaded green) and a region where AMPA broadband dominates (shaded orange). Depending on the kernel structure, this can produce relatively complex shape effects beyond slope changes.

Finally, even with multiple subprocesses, applying an identical 1/f-like filter across all subprocesses does not change the transition points between processes (Figure 3 Panel F).

This result shows that, under the FPP modeling regime, there is far more information represented in a neural power spectrum than merely narrowband oscllations or changes in 1/f-like slope in an otherwise uniform aperiodic spectral component. Rather, different frequency regions of the spectrum could reflect different subprocesses that have their own CIF and broadband components. In fact, it makes the prediction that the power spectrum could represent the emergence of different subprocesses dominating on different timescales, such as in the case of up- and down-states, which we explore in Result 4.

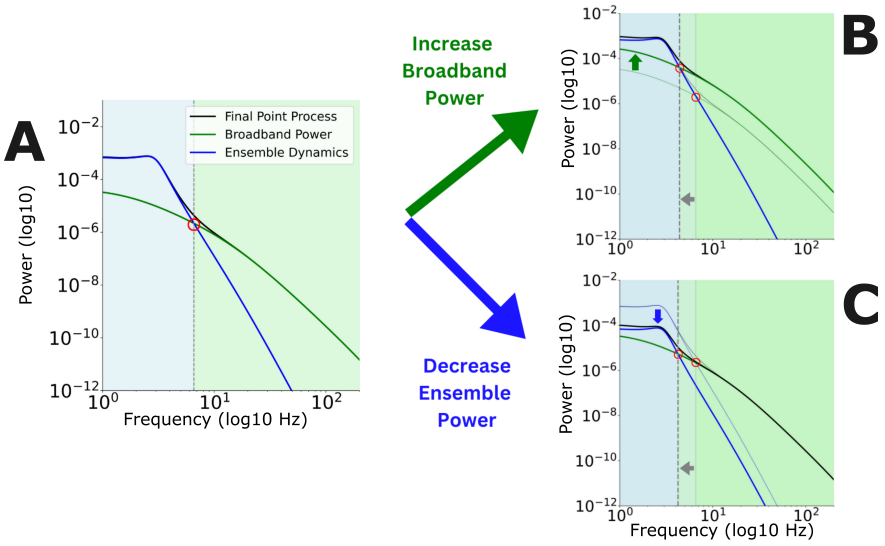


Figure 4: **Transition points between model components are determined by the relative magnitude between model components.** A) Shown are the spectral components of a Cox process with an AR(2) conditional intensity function (CIF) and a mean rate. The dominating component in the blue region is the spectrum of the CIF (blue line) and the dominating component in the green region is the mean rate (green line). The transition point takes place at $\sim$ 6.56 Hz. B) Keeping the spectrum of the CIF constant, an increase in the mean rate of the process moves the transition point to lower frequencies (4.39 Hz). Both transition points are circled in red and their relative movement of the transition points is highlighted by the gray array. The relative movement of the mean rate is highlighted by the green arrow. C) Keeping the mean rate of the process constant, a decrease in the power of the CIF spectrum (blue arrow) results in a shift of the transition point to lower frequencies (4.23 Hz). Movements in transition points suggest that different frequency regions of the power spectrum, even in the absence of rhythms, should be interpreted in a time-dependent manner with respect to the underlying dynamics.

**Result 3: Subprocess transition points are determined by the relative magnitude of ensemble dynamics and broadband**

In Result 1, it was shown that, given fixed ensemble dynamics and broadband parameters, transition points and dominant components do not change when filtering for a single subprocess. In Result 2, it was shown that additional transition points can emerge at the level of modeling subprocesses. Here, we show that changing the relative magnitude between model components at the level of a single subprocess shifts where transition points can occur–both within a subprocess and across interacting subprocesses.

As a case study, we show a single GABA subprocess with an AR(2) CIF in Figure 4 Panel A; it has already been filtered by both the GABA and 1/f-like filter and has a transition point established around 6.56 Hz. There are two ways that the transition point can shift: the broadband component can increase or decrease in power relative to ensemble dynamics or vice versa. In Panel B, the ensemble dynamics are kept constant and the broadband component is increased from 50 to 400 $spikes/sec$. This results in a shift of the transition point from around 6.56 Hz to 4.39 Hz, substantially increasing the impact of the broadband on the overall power spectral shape. Likewise, in Panel C, keeping the AR(2) coefficient the same and decreasing the AR(2) Gaussian (state) noise from 0.315 to 0.1 which induces a vertical and linear transformation across all frequencies, we see a shift from around 6.56 Hz to around 4.23 Hz. As such, relatively small changes in the relative magnitude of model components can have a large impact on the shape and interpretability of the power spectrum for given frequencies. Similarly, while shifting either component can produce comparable changes in the actual frequencies at which a given component is dominating the power spectrum, the final power spectra are different in their overall interpretation.

As a result, FPP models suggest that rhythmic information across brain states or tasks most likely is not contained in a fixed, relevant frequency band. Rather, the frequencies at which rhythmic or broadband information dominates can change drastically depending on the relative magnitudes of the ensemble dynamics versus broadband components. As such, tracking narrowband oscillation changes (e.g., traditional power analyses) or changes in frequency domain functional connectivity (e.g., Granger-Geweke causality analysis) across different global brain states or task structures could be ambiguous without using forward modeling to generate expectations for how frequencies of interest could

change. This is consistent with previous arguments presented in [19, 68, 2]. Furthermore, it suggests that smoothly shifting oscillations (e.g., drug infusion-induced changes) are not necessarily driven by changes in the mechanism of an oscillation itself but could be due to a stable oscillation that shifts in presentation as the broadband effects change. Forward models that can accurately account for both rhythmic and broadband information can be used to rule out such possibilities given knowledge of the underlying mechanisms.

**Result 4: FPP models capture both overall spectral structure and fine-timescale dynamics**

As described in the Theory section, FPP models are stationary, meaning that their statistical properties do not vary in time. This is one of the key features allowing for the full tractability of the modeling approach, which yields overall (i.e. long-timescale) theoretical power spectra. Nevertheless, for any given realization of the process, the instantaneous rate of events can be dynamic, i.e. the CIF $\lambda(t)$ can vary in time. If we condition on $\lambda(t)$, the resulting point process describing event times, $X(t|\lambda(t))$, is an inhomogeneous (i.e. non-stationary) Poisson process. We can use this property to study changes in the expected shape of the power spectrum on short timescales.

To study short-timescale dynamics, we will need to assume that $\lambda(t)$ is smooth or slowly varying, so that the rate of events is approximately constant in short time windows. This property is called semi-stationarity, and it is a common assumption when studying neural data using spectrograms [117, 118, 119]. By semi-stationarity, we can approximate the inhomogeneous Poisson process in a short time window by a homogeneous (i.e. constant-rate) Poisson process. We can then use the homogeneous Poisson process as the event process in our FPP model, deriving the theoretical power spectrum for that time window.

As a case study of this property, Figure 5 shows a bivariate Cox FPP model, derived in Equation 28, with AMPA and GABA subprocess components. The theoretical power spectrum (Panel A) shows the long timescale spectral shape, where the GABA subprocess dominates the power at frequencies below around 16 Hz and the AMPA subprocess dominates for higher frequencies. This is consistent with previous simulation work looking at AMPA and GABA processes interacting during propofol-induced unconsciousness [46], except here we've accounted for an additional narrow band slow wave rhythm that was not included in the prior work. We model the slow wave using a single Gaussian process with a spectral peak at 1 Hz: the AMPA and GABA CIFs multiply this process by 1.5 and -0.8, respectively.

We can study short-timescale properties in this model by generating a realization of the CIFs (Panel D), treating the process as semi-stationary, and investigating the properties of the time-varying theoretical power spectrum (Panels B, C, E, F, and G). In Panel D, it can be seen that the CIFs for AMPA and GABA oscillate at about 1 Hz, out of phase: the AMPA subprocess has an up-state when the GABA subprocess has a down-state and vice versa.

The semi-stationarity assumption allows us to study theoretical short-time power spectra at different time points (Panels B and C). At the peak of the AMPA process and the trough of the GABA process (Panel C), the overall spectral shape is dominated by AMPA power. At the trough of the AMPA process and the peak of the GABA process (Panel B), in contrast, frequencies below about 93 Hz are dominated by GABA power and higher frequencies are dominated by AMPA power. Hence the transition point between AMPA-dominated and GABA-dominated frequencies varies dynamically according to the phase of the rhythm, and even disappears when AMPA rates are high.

Note that the short timescale theoretical power spectra in Panels B and C are limited to frequencies above 10 Hz, while the long-timescale spectrum in Panel A has frequencies below 1 Hz. While we were able to compute these spectra at a single time point using the instantaneous model parameters, they are not truly instantaneous power spectra. Rather, they relate to time windows long enough for the CIFs to be "approximately constant". Here, the CIFs vary at about 1 Hz, so we assume that windows of about 100 ms have approximately constant rates: since the lowest resolvable frequency in a 100 ms window is 10 Hz, we truncate the power spectra at 10 Hz.

Also shown in Panels B and C are the spectral slope values at several selected frequencies. Importantly, the spectral slope is not the same across frequencies – for very high frequencies it converges to -6 (see Theory and supplemental derivations), but the slopes in the frequency range observed here have not converged to this limiting value. In other words, spectral slopes at frequencies typically studied in neuroscience research may have less to do with a theoretical limiting "power law", and more to do with the filter shapes of the component subprocesses and their relative magnitudes.

From these short-timescale power spectra, a theoretical spectrogram (Panel E) can be generated to build an intuition for how the resulting process would look as a function of time, changing dynamically as the balance of excitation to inhibition changes. By looking at the contours, we can see that the 1 Hz oscillation is affecting low and high frequencies differently: for low frequencies, power is higher when the GABA power is higher, while for high frequencies, power is higher when AMPA power is higher. In the middle, around 40 Hz, is a frequency were power is not affected much

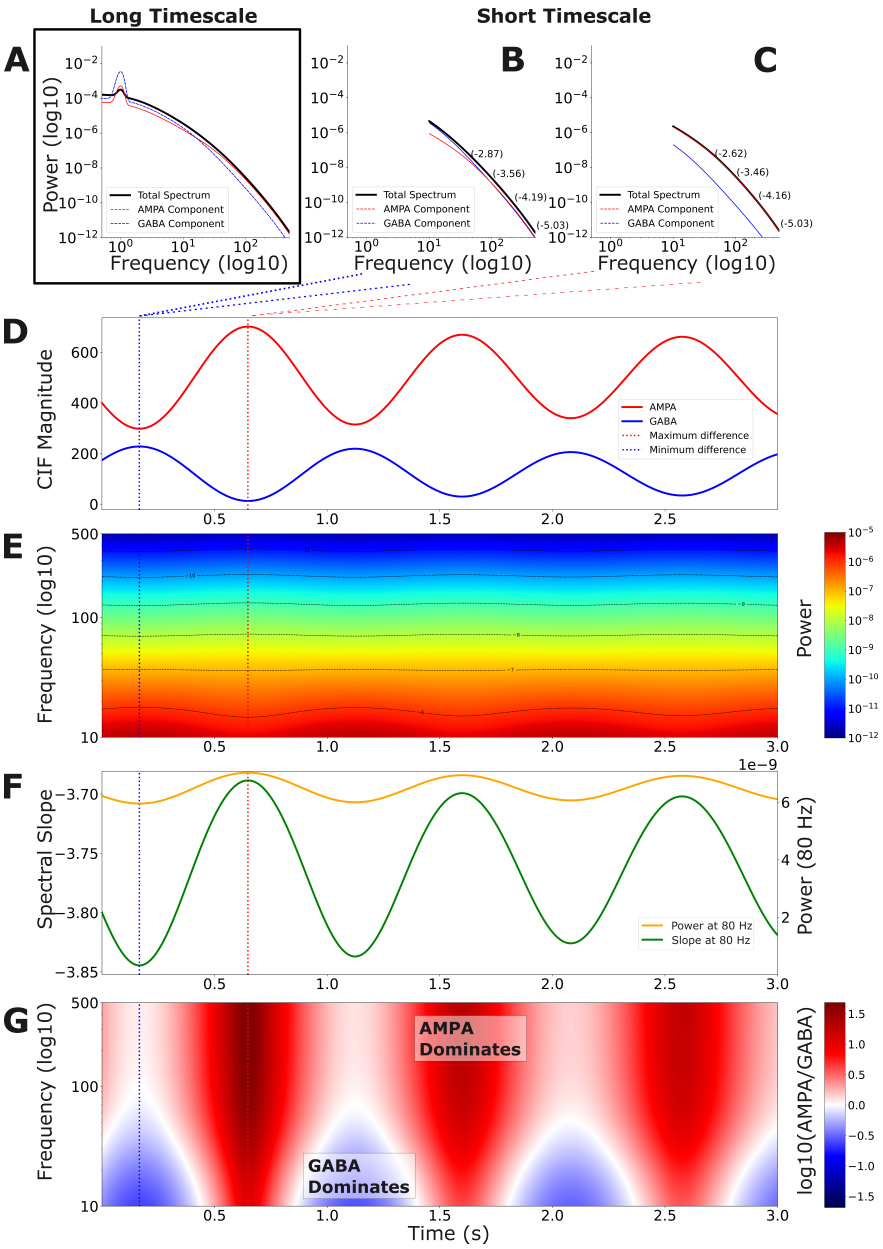


Figure 5: **Filtered point processes (FPPs) capture distinct information at different timescales.** (A) The theoretical power spectrum of a field potential modeled as a bivariate Cox process with AMPA and GABA subprocess components and a 1 Hz slow wave oscillation over a long timescale. The CIFs of each subprocess are identical up to a column vector that scales each CIF. (D) A single realization of the scaled CIFs for each subprocess for AMPA and GABA, respectively, and are then offset by the mean rate of each process. Assuming the realized conditional intensity function is semi-stationary on a short timescale, we can approximate higher frequencies of its power spectrum theoretically as a homogeneous Poisson process. (B) and (C) Two extremes where the AMPA and GABA CIFs are minimally and maximally distant in magnitude, respectively. This makes the prediction that the short-time power spectra will have periods where the overall spectral shape is dominated by primarily AMPA dynamics, whereas others will have lower frequencies dominated by GABA and higher frequencies are dominated by AMPA. Additionally, the spectral slope values at 40, 90, 200, 450 Hz for the total spectrum are shown, indicating that these models have not yet converged to the overall model limiting slope (see Supplemental Materials for derivation). (E) These semi-stationary dynamics at a fine timescale can be visualized across total time in the continuously varying theoretical spectrogram. (F) The spectral slope and power at 80Hz as a function of time. (G) The times and frequencies at which a given subprocess component is dominating the spectral shape can be highlighted by showing log ratio of AMPA and GABA components from the short-time spectrogram.

by the oscillation. In traditional terms, the spectral slope and high frequency broadband power are both changing dynamically during the rhythm (Panel F shows the spectral slope and power at 80 Hz).

The source of these effects is the changing relative contributions of the AMPA and GABA components: to facilitate interpretation, we show the time varying log ratio of the AMPA and GABA components (Panel G). This highlights the times and frequencies when the power spectrum is dominated by the AMPA component (red) or the GABA component (blue). We can also see the transition point between AMPA-dominated and GABA-dominated frequencies as a white band, varying dynamically from about 93 Hz at the peak of the GABA process to disappearing at the peak of the AMPA process. Hence we see from this example how the broadband components and the rhythm can *interact*: here, both the height and the shape of the overall power spectrum vary as a function of the rhythmic phase. For more complicated models, the changes in power spectral shape at short timescales could be even more complex.

This analysis of timescales makes a strong prediction, which is that cross-frequency coupling between rhythmic phase and broadband power should be ubiquitous in neural electrophysiological recordings. Under the model, every rhythmic component is accompanied by a broadband component for the same subprocess, and on short timescales the height of the broadband component will change dynamically with the phase of the rhythm. Of course, the broadband components may be obscured by larger components, for example when the GABA broadband component is obscured by the AMPA broadband component at the peak of the AMPA rhythm in Figure 5. In some situations, strong non-rhythmic broadband components may completely hide any cross-frequency coupling in weaker subprocesses. Nevertheless, this result predicts a very close relationship between rhythms and broadband power (and shape) that could be instrumental in interpreting cross-frequency coupling in biophysical terms.

Practically, this type of timescales analysis can be used to validate theoretical models of neural dynamics in comparison to data. For example, FPP models of rhythms can specify which synapse types participate in the rhythms at which phases; then long- and short-timescale model predictions can be compared to empirical spectra and spectrograms, using the entire spectral shape to assess model performance. Rhythmic-broadband interactions vary at sub-second or low-second timescales in multiple brain states [e.g., 120, 121, 122, 123]. This phenomenon has been called “spectral-switching" [e.g., 121, 122, 123]; FPPs could serve as a strong theoretical framework for studying the biophysical generators of these effects.

# Discussion

In this paper, we have presented a tractable probabilistic forward modeling framework that can explain rhythmic and broadband information in neural power spectra using filtered point processes (FPPs). Building on prior work modeling broadband effects in the power spectrum using random event times filtered by characteristic event shapes, we introduced dynamic event rates to account for rhythmic and time-varying ensemble firing rates, and we introduced multiple interacting subprocesses to account for different synapse types or populations in the modeled tissue. We showed that the theoretical power spectrum of the modeled field recordings remains tractable, and that it decomposes into narrowband and broadband components related to each subprocess (Equations 8 (one subprocess) and 23-28 (multiple subprocesses)). The resulting framework can be used to evaluate whether proposed biophysical mechanisms can explain observed spectral effects, including both rhythmic and broadband effects and their dynamic relationships.

## Insights and takeaways

Analysis of representative FPP models demonstrated that analyzing power spectral shape effects as a whole provides more accurate insights into the underlying biophysical dynamics of a recording than focusing on specific features or frequency ranges. In an FPP model, broadband and ensemble contributions to the power spectrum of a subprocess are modeled explicitly. This reveals transition points in the subprocess dominating the power spectrum. Thus, the modeling question shifts from needing knowledge of all relevant system information to modeling what has the largest impact on the power spectrum at a given frequency.

For a single subprocess, the transition point between the broadband component and the ensemble component is not affected by the event shape or subsequent filtering (Result 1), but it is affected by the relative power of the ensemble dynamics and the broadband (Result 3). For multiple subprocesses, event shapes become important: faster shapes (e.g. excitatory postsynaptic potentials or action potentials) will allow processes to dominate higher frequencies, while slower shapes (e.g. inhibitory postsynaptic potentials) will constrain processes to lower frequencies (Result 2), subject to the relative firing rates of the processes. Once the event shapes are fixed, additional filters do not change transition points. The transition points within and between subprocesses can also change dynamically in time (Result 4), and treating the process as semi-stationary can facilitate analysis of the spectral properties at short (e.g. sub-second) timescales. In other words, theoretical models of rhythms and the entrainment of population firing rates could be tested with FPPs

by making predictions of how power should be distributed across frequencies on both short and long timescales and comparing the predictions to empirical data.

These observations have important implications for researchers interpreting neural power spectra. First, the rhythmic and broadband components (and their interactions) add together to create the total power spectrum: this challenges popular spectral decomposition methods that decompose the power spectrum in log space, which effectively assume that the components have multiplicative effects on the power spectrum [68, 111].

Secondly, this additive relationship means that when viewed in log space, rhythmic dynamics and broadband will dominate the spectrum at different frequencies, and the spectral slope of the broadband component will be effectively invisible when analyzing slope in frequency regions dominated by rhythms. Thus, spectral slope analyses of the broadband component should be restricted to frequency ranges where there is not a known rhythm dominating the power spectrum. Similarly, there has been interest in the field about the spectral slope of low-frequency ensemble dynamics [113, 49, 114, 115, 116]: these analyses should also be restricted to frequencies where researchers do not expect other rhythms or broadband to be dominating.

Thirdly, our results caution against the use of static frequency ranges to assess the rhythmic power, broadband height, or spectral slope. Fixing predetermined oscillatory ranges (e.g., 8 - 12 Hz, 12 - 20 Hz) or broadband ranges (e.g., 80 - 200 Hz) for analysis can be misleading, since the relevant frequency ranges are likely to shift. Although this prediction would suggest that certain well-established power spectral analyses might need to be used with caution (which is consistent with previous work, e.g., [19, 20, 124, 125, 126, 127, 128]), analyzing the power spectrum as a whole provides a potentially useful perspective as a marker of changing brain states.

Finally, the FPP framework predicts that cross-frequency coupling between low-frequency rhythms and broadband spectral power and shape should be ubiquitous in neural electrophysiological recordings. If we believe that the primary contributors to the recordings are event-like (postsynaptic potentials, action potentials, etc.) and that rhythms reflect the ensemble dynamics of these events, then each rhythmic component of the power spectrum should be accompanied by a phase-locked broadband component at short timescales. While the cross-frequency coupling may be obscured by stronger dominant broadband components in some brain states, this close relationship between rhythmic and broadband power should be taken into account when interpreting cross-frequency coupling.

Altogether, our results predict that the overall shape of the power spectrum provides much more information about the underlying biophysical process than merely the rhythms, broadband height (e.g. high-gamma power) and power spectral slope. Rather, if researchers have prior knowledge about the dominant generators of a given LFP, ECoG, or EEG signal (e.g., given postsynaptic potentials, dendritic calcium spikes, local action potentials of a given cell type), which is already important for interpreting field potentials in a specific brain state [7], the entire power spectrum is interpretable beyond narrowband rhythms and a uniform broadband component [120, 121, 122, 123].

### Relationship to prior work

Neuroscience has a rich history of theoretical forward modeling, using mathematical models at the molecular, neuronal, circuit, population, and systems levels, to propose underlying mechanisms of observed dynamics and to make predictions to guide future experimental studies [129, 130, 131, 132]. In the context of modeling field potentials, conductance-based models have been used to model micro-scale extracellular potentials all the way up to scalp recordings [133, 134, 135, 136, 137]. In principle conductance-based models could account for broadband spectral effects [e.g., 138, 139] and could capture rhythmic and broadband effects simultaneously. However, as mentioned, these models often do not match the broadband spectral properties of observed neural signals [e.g., 65], because they emphasize low-frequency and narrowband rhythmic time series as model fit criteria. Modeling meso-scale broadband spectral effects using such fine-grained models is additionally difficult because of the dependence of broadband effects on the detailed spatial correlation structure across neurons, where empirical data are lacking.

There is also value in being able to generate theoretical models at higher spatial scales without the very fine level of granularity required for compartment-based neuronal modeling. Currently, two main approaches help to solve this issue: 1) single compartment neurons with conductances and 2) mean-field or neural mass models. Single compartment neurons, while often computationally tractable, often do not scale accurately to capture the empirical structure of ECoG or EEG recordings [140]. Mean-field models often focus on slow time-domain dynamics and narrowband rhythms over a mass of neural tissue [141, 142]; by design, they capture the dynamics of the population firing rate. As a result, mean-field models typically do not capture broadband power spectral features or effects because they mathematically assume the impact of autocovariance and cross-correlation on neural dynamics is negligible [82, 142]. With that in mind, mean-field models could be used in conjunction with FPP models, where they could be used in the place of the time-varying CIFs.

Filtered *homogeneous* point process models were introduced to address the limitations of previous rhythmic models and to capture broadband effects at higher spatial scales. We expect that by capturing both rhythmic and broadband components, and including multiple interacting subprocesses, FPP models will offer significantly more flexibility. The bivariate model of AMPA and GABA subprocesses has been of interest in many investigations over recent years in modeling ECoG and EEG [e.g., 46, 86, 28] and is now amenable to investigation with FPPs (Result 5). However, FPPs can also capture more general dependency between subprocesses (Equation 23).

The use case of FPP models that we described here takes the perspective of a recording electrode and models the multiple subprocesses that affect the recorded signal. As such, we have omitted literature using shot noise as input to model neurons or neural populations, which has focused primarily on fractal point processes as input to Fitzhugh-Nagumo and Hodgkin-Huxley models of peripheral nerves and neurons using renewal processes (reviewed in [143] e.g., [144, 145]. We also omit the body of literature reviewed and developed in [146], where they introduce "fractal shot noise processes," which is a special instance of our more general framework.

Finally, we note the theoretical power spectrum for a Cox process has been well characterized in the measure-theoretic probability literature for some time [e.g., 92, 90, 91] and the theoretical power spectrum for a homogeneous Poisson process has been well characterized for use in neuroscience before [e.g., 29, 74]; however, because many recent theoretical analyses have simulated FPPs in the time domain before estimating the power spectrum nonparametrically for model analysis [46, 86], we directly provide the theoretical power spectra for a given model structure. Additionally, we provide a software package called `filtered_point_process` with simple tutorials to demonstrate how to use the framework (github repository: https://github.com/Stephen-Lab-BU/filtered-point-process).

## Limitations and Future Directions

The FPP models assume that the subprocess events sum linearly in their contribution to the recording electrode, and that the waveform shapes do not vary as a function of time or location. This is a strong assumption and clear examples exist where it does not hold. For example, postsynaptic potential shapes vary based on the time-varying intracellular potential of the electrode [130] and on the relative location of the synapse from the recording electrode [147, 148, 149]. Because our subprocesses are intended to capture many different synapses on many different neurons in the vicinity of the electrode, this could lead to significant errors in the calculation of the theoretical power spectrum. We described in the Theory section how valuable FHPP models have been to the scientific literature despite sharing this limitation. Nevertheless, in future work we plan to use nonlinear compartment-based models of cortex to evaluate the size of the effect that these approximations have on the power spectrum in specific modeled brain states. Then, we will investigate ways to alter the models to improve their performance.

For example, elegant theoretical work in integrate and fire model neurons has recently derived theoretical power spectra for the output of model neurons with nonlinear responses [150], and our framework could benefit from incorporating elements of this approach into our models. We expect that in certain brain states, it will also be important to account for variation in waveform shape across time and space. A state space model could capture time-dependence by allowing the waveform shape to change depending on the level of the CIF of the process. For the dependence on space, we could model the waveform shape as stochastic [151], as in generalized shot noise models, which could be useful for capturing variability in power spectra across a grid of electrodes (e.g., Utah arrays) driven by the positioning of a dipole source relative to the electrode position. Alternatively, it is possible to estimate effective linear waveforms across space, either theoretically using conductance-based compartment models [152, 147], or empirically as in recent work on unitary LFPs, which estimate the impact of a single axon on the local LFP [149, 100, 153]. Incorporating these empirical waveforms into the FPP framework could yield spectral estimates that are more accurate than the theoretical filters used here.

Our models do not account for refractory periods or self-history, which can have a significant effect on the power spectrum even when summed across neurons or synapses [154]. The FPP models can account for such effects by using renewal point processes or Cox processes with self-history dependence as the event time process, because the theoretical power spectra and cross-spectra of these processes are tractable [155, 156]. Interestingly, refractory periods typically have the effect of reducing low-frequency power relative to higher frequencies, regardless of the presence of low-frequency rhythms [155, 156, 5, 157], and these effects persist in the sum across neurons or synapses [154]. To our knowledge, this effect is never observed in empirical neural power spectra of field recordings, which tend to have the highest power at low frequencies. In other words, FPP models with a refractory period would likely have lower power at very low frequencies than high frequencies, which does not match empirical observations. FPP models could be built and adapted to study this paradox.

Our models are stationary, meaning that the overall properties of the models do not depend on time. While the semi-stationarity assumption can be used to study fine-timescale dynamics in the power spectrum by conditioning on

the dynamic CIFs, even when the overall model is stationary, there will be some scientific questions where the stationary assumption is not appropriate. For example, different sleep stages are characterized by categorically different rhythms, and it would not make sense to use a single FPP model for all stages. In cases like these, a switching state-space approach could be used in which a discrete hidden state (e.g. the current sleep stage) controls which subprocesses and rhythms are in effect. Switching state space models have been used to great effect in modeling non-stationary power spectral effects in neuroscience [67, 158, 69].

Finally, the FPP framework is currently a probabilistic *forward* model and does not provide methods for parameter estimation, i.e. we do not yet describe how the model parameters can be estimated statistically from data. The general model framework does not guarantee that any particular model is identifiable, so there may not be enough information in a dataset to fit any particular model. In the future, we will describe principles for designing identifiable FPP models for specific brain states or neural dynamics that are simple enough to be fit to empirical data, and we will present methods for fitting such models. We believe FPPs will be a useful statistical model for empirically driven spectral decomposition, and our future work will develop the estimators, goodness-of-fit metrics, and ground-truth validation required for a successful statistical framework.

By bridging the gap between micro-scale biophysics and macro-scale narrowband and broadband biomarkers, our modeling framework enables theoretical modeling of the rapidly growing collection of known narrowband and broadband changes in healthy and diseased brain states. These theoretical models, and the software packages implementing them, can be used to improve the interpretability of neural power spectra for scientific and clinical progress.

# Materials and Methods

The FPP framework described above allows for time-varying rates by modeling the CIF $\lambda(t)$ of each process as a Gaussian process with a known power spectrum $S_\lambda(f)$ (Equation 1 for a single process and Equation 16 for multiple subprocesses). We use two different types of Gaussian processes: (1) spectrally-defined Gaussian processes, where the process is defined by its mean and power spectrum (first and second moments), and (2) autoregressive (AR) processes, where the process is defined based on its dependence on previous time lags. We present each below, and then describe how each is used in the example models used in the Results.

## Spectrally-defined Gaussian Process CIFs

For spectrally-defined Gaussian processes, we choose the power spectrum of the desired CIF $S_\lambda(f)$ . While the spectrum of a Gaussian process can be any well behaved shape, we chose to represent narrowband rhythms as Gaussian shapes or bell curves. In order to allow for multiple rhythms, the spectrum of the process is defined as having an arbitrary number of Gaussian shapes:

$$S_\lambda(f) = \sum_i A_i \cdot \exp\left(-\frac{(f-\mu_i)^2}{2\sigma_i^2}\right) \tag{29}$$

where $f$ frequency; the $i$-th Gaussian peak is defined by a mean $\mu_i$ (center frequency), standard deviation $\sigma_i$ (frequency width), and amplitude $A_i$ (peak height).

## Autoregressive Process CIFs

Another type of Gaussian process that can be useful for modeling the CIF is a discrete time autoregressive process, which models the current time point as a function of $p$ previous time points (referred to as an AR($p$) process) [4]:

$$\lambda_k^{AR} = \sum_{j=1}^{p} \alpha_j \lambda_{k-j}^{AR} + \epsilon \tag{30}$$

where the index $k$ in $\lambda_k^{AR}$ refers to the time bin, as in $\lambda(k\Delta t)$, and $\epsilon$ is white Gaussian noise with variance $\sigma^2$. We assume that the model coefficients $\alpha_j$ are chosen so that the process is stable. The power spectrum of the process is:

$$S_\lambda^{AR}(f) = \frac{\sigma^2 \Delta t}{\left|1 - \sum_{j=1}^{p} \alpha_j e^{-ij2\pi f}\right|^2} \tag{31}$$

[4]. With this power spectrum and a mean rate $\lambda_0$, we can use Equations 1-2 to define a Cox process with an Autoregressive CIF. In the case $p = 1$ the power spectrum only has a peak at 0 Hz and proceeds to decrease monotonically, which means it does not have rhythms. This case represents a discrete-time random walk, and it can be useful for modeling ensemble dynamics that vary smoothly in time without oscillating.

We generalize this result to account for multivariate AR processes. Consider the case where the CIFs obey a multivariate AR process of order 1, i.e.:

$$\vec{\lambda}(t) = A\vec{\lambda}(t-1) + \vec{\epsilon} \tag{32}$$

where $A$ is a transition matrix and $\vec{\epsilon}$ is multivariate zero-mean Gaussian noise with covariance $\Sigma$. If we assume that the process is stable, then the cross-spectrum of the process is [3]:

$$\begin{aligned} C_{\vec{\lambda}}(f) &= \frac{1}{2\pi}\Gamma(f)\Sigma\Gamma^\dagger(f) \\ \Gamma(f) &= (I - Ae^{-i2\pi f})^{-1} \end{aligned} \tag{33}$$

where † denotes the conjugate transpose. Note the similarity between this theoretical cross-spectrum and the spectrum of a univariate AR process given in Equation 31, where the variance $\sigma^2$ has been replaced by the covariance $\Sigma$ and the square in the denominator has been replaced by pre- and post-multiplying by $\Gamma$. This cross-spectrum can be used in Equations 19-23 to compute the field spectrum.

## Models used in the Results

### Figure 2

In Figure 2, we model the CIF using a spectrally-defined Gaussian process with mean, $\lambda_0$, of 500 $spikes/sec$ and power spectrum $S_\lambda(f)$, where we construct the power spectrum to have a rhythm (which we modeled as a Gaussian-shaped bump using Equation 29) with width 0.1 Hz centered at 1 Hz and a height of 5000 $spikes/sec$. Defining the process using its frequency domain second moment (its power spectrum) is convenient in this context, because we focus mainly on the power spectral properties of the model. The equations for the model are specified as the following for each step: for Figure 2 Panel C, Equation 3 (left) and Equation 4 (right), for Panel F Equation 7 (left) and Equation 8 (right) where $\tau_{rise}$ = 0.4 ms and $\tau_{decay}$ = 10 ms to represent a GABA PSP, and for Panel I Equation 13 (left) and Equation 8 (right) where $\tau_{LP}$ = 10 ms.

For interpretability, the y-axis scaling in Panel C is linear in units of $spikes/sec$. This is conventional for point process power spectra [5, 157] and aids in identifying mean rate as the height of the flat component ($\lambda_0$ in Equation 4). The y-axis scaling for Panels F and I uses the convention for continuous stochastic processes, $power/Hz$ (e.g. $\mu V^2/Hz$), which differs from the point process scaling by a factor of $(\Delta t)^2$ [156, 157]. We use these conventions throughout.

The CIF described above was simulated to give a realization of Equation 3 through the approximate frequency domain method outlined in [3]. A realization of the corresponding point process was created via the standard "thinning" procedure for inhomogeneous Poisson processes [159]; this is highly efficient and is justified provided an intensity is continuous and bounded for any finite interval.

Shaded in gray in Panel F and Panel I is a multitaper estimate of 60 seconds of simulated data (a snippet is shown in the left of the figure) with a frequency resolution of 0.133 Hz. This shows that direct estimation from the simulated data correctly recovers the intended theoretical power spectrum. All parameters are summarized in table 4.

### Figure 3

In Figure 3 Panels A-C (Result 1), a single subprocess is modeled as a Cox FPP with a spectrum given by Equation 4. The CIF is represented as an AR(2) process, given by Equation 31. Panel A is the unfiltered point process spectrum, Panel B is the unfiltered point process spectrum shaped by the magnitude squared of a PSP filter given in Equation 9 with $\tau_{decay} = 10$ ms and $\tau_{rise} = 0.4$ ms, which represents a GABA kernel. Panel C multiplies the filtered spectrum in panel B by the squared magnitude of the lowpass filter given in Equation 12, where $\tau_{LP} = 10$ ms. All parameters are summarized in table 5.

Similarly, in Figure 3 Panels D-F (Result 2) two subprocesses are modeled: process 1 and process 2. Each process spectrum is unfiltered in Panel D. In panel E, process 1 is filtered with an AMPA waveform and process 2 is filtered with a GABA waveform; additional low-pass filter was applied to each subprocess (Panel F), as was done for the single subprocess. For the GABA process, the unfiltered spectrum is given by an AR(2) process and the AMPA process is modeled as an AR(2) process, both with $fs = 1000$ Hz. All parameters are summarized in table 6. Note that the $\sigma^2$ parameter is marginally offset between each process to avoid perfect overlap to demonstrate the effect of interest; the $\sigma^2$ also induces a vertical shift. Panel E and F are identical to the filtering done in Panel B and C, except with the addition of the AMPA kernel given in Equation 9 with $\tau_{decay} = 4$ ms and $\tau_{rise} = 0.4$ ms.

### Figure 4

In Figure 4 (Result 3), a Cox FPP is modeled using an AR(2) CIF, a GABA filter, and a low-pass filter where both filters are identical to those described in Results 1-2. In Panel A, the AR(2) CIF has noise variance $\sigma^2 = 0.315$, and the mean rate of the process $\lambda_0$ is 50 $spikes/sec$. Panel B keeps all parameters the same as Panel A, except the broadband component $\lambda_0$ is increased to 400 $spikes/sec$. Panel C keeps all parameters the same as Panel A, except decreases the CIF (ensemble power) to $\sigma^2 = 0.1$. All parameters are summarized in table 7.

### Figure 5

In Figure 5 (Result 4), the CIFs of the subprocesses are shared up to a linear transform (given by Equation 27 with $w_A = 1.5$, $w_G = -0.8$, $\lambda_0^A = 500$, and $\lambda_0^G = 100$), where the shared process ($\lambda(t)$) is a spectrally-defined Gaussian process with a rhythmic peak at 1 Hz and peak power of 5000 $spikes/sec$. An additional low-pass filter is also used, as with Figure 2. The filters are given as $\tau_{\text{rise,GABA}} = 0.4$ ms and $\tau_{\text{decay,GABA}} = 10$ ms and $\tau_{\text{rise,AMPA}} = 0.4$ ms and $\tau_{\text{decay,AMPA}} = 4$ ms. The low-pass filter is defined with $\tau_{LP}$ = 10 ms. The resulting power spectrum captures long timescale dynamics. All parameters are summarized in table 8.

Short timescale spectra are captured by generating a realization of the CIF for each subprocess. Conditioning on that realization $\lambda(t)$, semi-stationarity can be assumed within small windows, so that the point process power spectra $S_{X,A}|\lambda_A(t)$ and $S_{X,G}|\lambda_G(t)$ are approximately homogeneous, and equal to the rate at that time ($\lambda_A(t)$ and $\lambda_G(t)$, respectively). Conditioned on the rate, the two point processes are independent. After applying the postsynaptic filters and the low-pass filter, the cross-spectrum of the components is:

$$C_{Y,AG}|\lambda(t) = \begin{bmatrix} |\mathcal{H}^{LP}|^2|\mathcal{H}^A|^2\lambda_A(t) & 0 \\ 0 & |\mathcal{H}^{LP}|^2|\mathcal{H}^G|^2\lambda_G(t) \end{bmatrix} \tag{34}$$

and the total power spectrum is:

$$\begin{aligned} S^{LP}_{field}|\lambda(t) &= |\mathcal{H}^{LP}|^2|\mathcal{H}^A|^2\lambda_A(t) \\ &\quad +|\mathcal{H}^{LP}|^2|\mathcal{H}^G|^2\lambda_G(t) \end{aligned} \tag{35}$$

Panels B and C show the total spectrum and AMPA and GABA components (diagonals of Equation 34) for two chosen time points, and Panel E shows the total spectrum as a function of time (a spectrogram). Panel F shows the spectral slope and power at 80Hz as a function of time. Panel G shows the log ratio of the AMPA and GABA components from the spectrogram from E, i.e. $\log(S_{Y,A}(f)/S_{Y,G}(f))$, where $S_{Y,A}(f)$ and $S_{Y,G}(f)$ are the diagonals of Equation 34.

## Implementation

The FFP framework, figure Jupyter notebooks, and all models were implemented in custom Python code and are available on the publicly available github package 'filtered-point-process' https://github.com/Stephen-Lab-BU/filtered-point-process)–an actively managed software package that will continue to be expanded in available features and tutorials.

## Acknowledgments

We'd like to thank the following individuals for valuable feedback: John Tauber, Becky Belisle, Proloy Das, Mingjian Alex He, Mark Kramer, and Uri Eden. We'd also like to thank the following funding opportunities: (Stephen) the Boston University Department for Mathematics and Statistics and the Boston University Center for Systems Neuroscience, (Oyama) the Boston University Undergraduate Research Opportunities Program, and (Bloniasz) NIH NINDS JSTPN T32NS131178 in early stage neuroscience, the NSF GRFP (2234657), and the Graduate Program for Neuroscience (GPN).

# References


[1] Jeremy R Manning, Joshua Jacobs, Itzhak Fried, and Michael J Kahana. Broadband shifts in local field potential power spectra are correlated with single-neuron spiking in humans. *The Journal of neuroscience: the official journal of the Society for Neuroscience*, 29(43):13613–13620, 28 October 2009. doi: 10.1523/JNEUROSCI.2041-09.2009.

[2] Thomas Donoghue and Andrew J Watrous. How Can We Differentiate Narrow-Band Oscillations from Aperiodic Activity? In Nikolai Axmacher, editor, *Intracranial EEG: A Guide for Cognitive Neuroscientists*, pages 351–364. Springer International Publishing, Cham, 2023. doi: 10.1007/978-3-031-20910-9_22.

[3] M B Priestley. *Spectral Analysis and Time Series, Two-Volume Set: Volumes I and II*. Elsevier Science, 1982.

[4] Donald B Percival and Andrew T Walden. *Spectral Analysis for Physical Applications*. Cambridge University Press, 3 June 1993. doi: 10.1017/CBO9780511622762.

[5] Robert E Kass, Uri T Eden, and Emery N Brown. *Analysis of Neural Data*. Springer New York, 2014. doi: 10.1007/978-1-4614-9602-1.

[6] György Buzsáki, Costas A Anastassiou, and Christof Koch. The origin of extracellular fields and currents–EEG, ECoG, LFP and spikes. *Nature reviews. Neuroscience*, 13(6):407–420, 18 May 2012. doi: 10.1038/nrn3241.

[7] Alain Destexhe and Claude Bédard. Local Field Potentials: LFP. In Dieter Jaeger and Ranu Jung, editors, *Encyclopedia of Computational Neuroscience*, pages 1903–1914. Springer New York, New York, NY, 2022. doi: 10.1007/978-1-0716-1006-0_548.

[8] Hans Berger. Über das Elektrenkephalogramm des Menschen. *Archiv für Psychiatrie und Nervenkrankheiten*, 87 (1):527–570, 1 December 1929. doi: 10.1007/BF01797193.

[9] A K Engel, P Fries, and W Singer. Dynamic predictions: oscillations and synchrony in top-down processing. *Nature reviews. Neuroscience*, 2(10):704–716, October 2001. doi: 10.1038/35094565.

[10] György Buzsáki and Andreas Draguhn. Neuronal oscillations in cortical networks. *Science*, 304(5679):1926–1929, 25 June 2004. doi: 10.1126/science.1099745.

[11] György Buzsáki. *Rhythms of the Brain*. Oxford University Press, 2006.

[12] György Buzsáki, Nikos Logothetis, and Wolf Singer. Scaling brain size, keeping timing: evolutionary preservation of brain rhythms. *Neuron*, 80(3):751–764, 30 October 2013. doi: 10.1016/j.neuron.2013.10.002.

[13] Nancy Kopell, Mark A Kramer, Paola Malerba, and Miles A Whittington. Are different rhythms good for different functions? *Frontiers in human neuroscience*, 4:187, 2 November 2010. doi: 10.3389/fnhum.2010.00187.

[14] Pascal Fries. Rhythms for Cognition: Communication through Coherence. *Neuron*, 88(1):220–235, 7 October 2015. doi: 10.1016/j.neuron.2015.09.034.

[15] Mathilde Bonnefond, Sabine Kastner, and Ole Jensen. Communication between Brain Areas Based on Nested Oscillations. *eNeuro*, 4(2), 27 March 2017. doi: 10.1523/ENEURO.0153-16.2017.

[16] Samuel P Burns, Dajun Xing, and Robert M Shapley. Is gamma-band activity in the local field potential of V1 cortex a "clock" or filtered noise? *The Journal of neuroscience: the official journal of the Society for Neuroscience*, 31(26):9658–9664, 29 June 2011. doi: 10.1523/JNEUROSCI.0660-11.2011.

[17] Freek van Ede, Andrew J Quinn, Mark W Woolrich, and Anna C Nobre. Neural Oscillations: Sustained Rhythms or Transient Burst-Events? *Trends in neurosciences*, 41(7):415–417, July 2018. doi: 10.1016/j.tins.2018.04.004.

[18] Scott R Cole and Bradley Voytek. Brain Oscillations and the Importance of Waveform Shape. *Trends in cognitive sciences*, 21(2):137–149, February 2017. doi: 10.1016/j.tics.2016.12.008.

[19] Stephanie R Jones. When brain rhythms aren't 'rhythmic': implication for their mechanisms and meaning. *Current opinion in neurobiology*, 40:72–80, October 2016. doi: 10.1016/j.conb.2016.06.010.

[20] Keith B Doelling and M Florencia Assaneo. Neural oscillations are a start toward understanding brain activity rather than the end. *PLoS biology*, 19(5):e3001234, May 2021. doi: 10.1371/journal.pbio.3001234.

[21] Thomas Donoghue, Natalie Schaworonkow, and Bradley Voytek. Methodological considerations for studying neural oscillations. *The European journal of neuroscience*, 55(11-12):3502–3527, June 2022. doi: 10.1111/ejn.15361.

[22] T H Bullock, M C Mcclune, and J T Enright. Are the electroencephalograms mainly rhythmic? Assessment of periodicity in wide-band time series. *Neuroscience*, 121(1):233–252, 2003. doi: 10.1016/s0306-4522(03)00208-2.

[23] K J Miller, S Zanos, E E Fetz, M den Nijs, and J G Ojemann. Decoupling the cortical power spectrum reveals real-time representation of individual finger movements in humans. *The Journal of neuroscience: the official journal of the Society for Neuroscience*, 29(10):3132–3137, 11 March 2009. doi: 10.1523/JNEUROSCI.5506-08.2009.

[24] Kai J Miller. Broadband spectral change: evidence for a macroscale correlate of population firing rate? *The Journal of neuroscience: the official journal of the Society for Neuroscience*, 30(19):6477–6479, 12 May 2010. doi: 10.1523/JNEUROSCI.6401-09.2010.

[25] Supratim Ray and John H R Maunsell. Different origins of gamma rhythm and high-gamma activity in macaque visual cortex. *PLoS biology*, 9(4):e1000610, April 2011. doi: 10.1371/journal.pbio.1000610.

[26] Kai J Miller, Christopher J Honey, Dora Hermes, Rajesh P N Rao, Marcel denNijs, and Jeffrey G Ojemann. Broadband changes in the cortical surface potential track activation of functionally diverse neuronal populations. *NeuroImage*, 85 Pt 2(0 2):711–720, 15 January 2014. doi: 10.1016/j.neuroimage.2013.08.070.

[27] Máté Gyurkovics, Grace M Clements, Kathy A Low, Monica Fabiani, and Gabriele Gratton. Stimulus-Induced Changes in 1/f-like Background Activity in EEG. *The Journal of neuroscience: the official journal of the Society for Neuroscience*, 42(37):7144–7151, 14 September 2022. doi: 10.1523/JNEUROSCI.0414-22.2022.

[28] Niklas Brake, Flavie Duc, Alexander Rokos, Francis Arseneau, Shiva Shahiri, Anmar Khadra, and Gilles Plourde. A neurophysiological basis for aperiodic EEG and the background spectral trend. *Nature communications*, 15(1): 1514, 19 February 2024. doi: 10.1038/s41467-024-45922-8.

[29] C Bédard, H Kröger, and A Destexhe. Does the 1/f frequency scaling of brain signals reflect self-organized critical states? *Physical review letters*, 97(11):118102, 15 September 2006. doi: 10.1103/PhysRevLett.97.118102.

[30] Christopher T Kello, Gordon D A Brown, Ramon Ferrer-I-Cancho, John G Holden, Klaus Linkenkaer-Hansen, Theo Rhodes, and Guy C Van Orden. Scaling laws in cognitive sciences. *Trends in cognitive sciences*, 14(5): 223–232, May 2010. doi: 10.1016/j.tics.2010.02.005.

[31] Biyu J He. Scale-free brain activity: past, present, and future. *Trends in cognitive sciences*, 18(9):480–487, September 2014. doi: 10.1016/j.tics.2014.04.003.

[32] Kai J Miller, Larry B Sorensen, Jeffrey G Ojemann, and Marcel den Nijs. Power-law scaling in the brain surface electric potential. *PLoS computational biology*, 5(12):e1000609, December 2009. doi: 10.1371/journal.pcbi.1000609.

[33] W S Pritchard. The brain in fractal time: 1/f-like power spectrum scaling of the human electroencephalogram. *The International journal of neuroscience*, 66(1-2):119–129, September 1992. doi: 10.3109/00207459208999796.

[34] Moritz Gerster, Gunnar Waterstraat, Vladimir Litvak, Klaus Lehnertz, Alfons Schnitzler, Esther Florin, Gabriel Curio, and Vadim Nikulin. Separating Neural Oscillations from Aperiodic 1/f Activity: Challenges and Recommendations. *Neuroinformatics*, 20(4):991–1012, October 2022. doi: 10.1007/s12021-022-09581-8.

[35] Robson Scheffer-Teixeira, Hindiael Belchior, Richardson N Leão, Sidarta Ribeiro, and Adriano B L Tort. On high-frequency field oscillations (>100 Hz) and the spectral leakage of spiking activity. *The Journal of neuroscience: the official journal of the Society for Neuroscience*, 33(4):1535–1539, 23 January 2013. doi: 10.1523/JNEUROSCI.4217-12.2013.

[36] N E Crone, D L Miglioretti, B Gordon, J M Sieracki, M T Wilson, S Uematsu, and R P Lesser. Functional mapping of human sensorimotor cortex with electrocorticographic spectral analysis. I. Alpha and beta event-related desynchronization. *Brain: a journal of neurology*, 121 ( Pt 12):2271–2299, December 1998. doi: 10.1093/brain/121.12.2271.

[37] Eveline A Crone, Sarah E Donohue, Ryan Honomichl, Carter Wendelken, and Silvia A Bunge. Brain regions mediating flexible rule use during development. *The Journal of neuroscience: the official journal of the Society for Neuroscience*, 26(43):11239–11247, 25 October 2006. doi: 10.1523/JNEUROSCI.2165-06.2006.

[38] Alon Sinai, Christopher W Bowers, Ciprian M Crainiceanu, Dana Boatman, Barry Gordon, Ronald P Lesser, Frederick A Lenz, and Nathan E Crone. Electrocorticographic high gamma activity versus electrical cortical stimulation mapping of naming. *Brain: a journal of neurology*, 128(Pt 7):1556–1570, July 2005. doi: 10.1093/brain/awh491.

[39] Kai J Miller, Dora Hermes, and Nathan P Staff. The current state of electrocorticography-based brain-computer interfaces. *Neurosurgical focus*, 49(1):E2, July 2020. doi: 10.3171/2020.4.FOCUS20185.

[40] Edward F Chang. Towards large-scale, human-based, mesoscopic neurotechnologies. *Neuron*, 86(1):68–78, 8 April 2015. doi: 10.1016/j.neuron.2015.03.037.

[41] Maximilian E Dougherty, Anh P Q Nguyen, Vyassa L Baratham, and Kristofer E Bouchard. Laminar origin of evoked ECoG high-gamma activity. In *2019 41st Annual International Conference of the IEEE Engineering in Medicine and Biology Society (EMBC)*, pages 4391–4394. IEEE, July 2019. doi: 10.1109/EMBC.2019.8856786.

[42] Agrita Dubey and Supratim Ray. Comparison of tuning properties of gamma and high-gamma power in local field potential (LFP) versus electrocorticogram (ECoG) in visual cortex. *Scientific reports*, 10(1):5422, 25 March 2020. doi: 10.1038/s41598-020-61961-9.

[43] Supratim Ray, Nathan E Crone, Ernst Niebur, Piotr J Franaszczuk, and Steven S Hsiao. Neural correlates of high-gamma oscillations (60-200 Hz) in macaque local field potentials and their potential implications in electrocorticography. *The Journal of neuroscience: the official journal of the Society for Neuroscience*, 28(45): 11526–11536, 5 November 2008. doi: 10.1523/JNEUROSCI.2848-08.2008.

[44] Marcin Leszczyński, Annamaria Barczak, Yoshinao Kajikawa, Istvan Ulbert, Arnaud Y Falchier, Idan Tal, Saskia Haegens, Lucia Melloni, Robert T Knight, and Charles E Schroeder. Dissociation of broadband high-frequency activity and neuronal firing in the neocortex. *Science advances*, 6(33):eabb0977, August 2020. doi: 10.1126/sciadv.abb0977.

[45] Mototaka Suzuki and Matthew E Larkum. Dendritic calcium spikes are clearly detectable at the cortical surface. *Nature communications*, 8(1):276, 17 August 2017. doi: 10.1038/s41467-017-00282-4.

[46] Richard Gao, Erik J Peterson, and Bradley Voytek. Inferring synaptic excitation/inhibition balance from field potentials. *NeuroImage*, 158:70–78, September 2017. doi: 10.1016/j.neuroimage.2017.06.078.

[47] Vicente Medel, Martín Irani, Nicolás Crossley, Tomás Ossandón, and Gonzalo Boncompte. Complexity and 1/f slope jointly reflect brain states. *Scientific reports*, 13(1):21700, 7 December 2023. doi: 10.1038/s41598-023-47316-0.

[48] Bradley Voytek, Mark A Kramer, John Case, Kyle Q Lepage, Zechari R Tempesta, Robert T Knight, and Adam Gazzaley. Age-Related Changes in 1/f Neural Electrophysiological Noise. *The Journal of neuroscience: the official journal of the Society for Neuroscience*, 35(38):13257–13265, 23 September 2015. doi: 10.1523/JNEUROSCI.2332-14.2015.

[49] Róbert Bódizs, Orsolya Szalárdy, Csenge Horváth, Péter P Ujma, Ferenc Gombos, Péter Simor, Adrián Pótári, Marcel Zeising, Axel Steiger, and Martin Dresler. A set of composite, non-redundant EEG measures of NREM sleep based on the power law scaling of the Fourier spectrum. *Scientific reports*, 11(1):2041, 21 January 2021. doi: 10.1038/s41598-021-81230-7.

[50] S Dave, T A Brothers, and T Y Swaab. 1/f neural noise and electrophysiological indices of contextual prediction in aging. *Brain research*, 1691:34–43, 15 July 2018. doi: 10.1016/j.brainres.2018.04.007.

[51] Leonhard Waschke, Malte Wöstmann, and Jonas Obleser. States and traits of neural irregularity in the age-varying human brain. *Scientific reports*, 7(1):17381, 12 December 2017. doi: 10.1038/s41598-017-17766-4.

[52] Dillan Cellier, Justin Riddle, Isaac Petersen, and Kai Hwang. The development of theta and alpha neural oscillations from ages 3 to 24 years. *Developmental cognitive neuroscience*, 50:100969, August 2021. doi: 10.1016/j.dcn.2021.100969.

[53] Natalie Schaworonkow and Bradley Voytek. Longitudinal changes in aperiodic and periodic activity in electrophysiological recordings in the first seven months of life. *Developmental cognitive neuroscience*, 47:100895, February 2021. doi: 10.1016/j.dcn.2020.100895.

[54] T Inouye, Y Matsumoto, K Shinosaki, A Iyama, and S Toi. Increases in the power spectral slope of background electroencephalogram just prior to asymmetric spike and wave complexes in epileptic patients. *Neuroscience letters*, 173(1-2):197–200, 23 May 1994. doi: 10.1016/0304-3940(94)90182-1.

[55] Saskia van Heumen, Jeremy T Moreau, Elisabeth Simard-Tremblay, Steffen Albrecht, Roy Wr Dudley, and Sylvain Baillet. Case Report: Aperiodic Fluctuations of Neural Activity in the Ictal MEG of a Child With Drug-Resistant Fronto-Temporal Epilepsy. *Frontiers in human neuroscience*, 15:646426, 4 March 2021. doi: 10.3389/fnhum.2021.646426.

[56] Stavros Trakoshis, Pablo Martínez-Cañada, Federico Rocchi, Carola Canella, Wonsang You, Bhismadev Chakrabarti, Amber Nv Ruigrok, Edward T Bullmore, John Suckling, Marija Markicevic, Valerio Zerbi, MRC AIMS Consortium, Simon Baron-Cohen, Alessandro Gozzi, Meng-Chuan Lai, Stefano Panzeri, and Michael V Lombardo. Intrinsic excitation-inhibition imbalance affects medial prefrontal cortex differently in autistic men versus women. *eLife*, 9, 4 August 2020. doi: 10.7554/eLife.55684.

[57] Nataliia Kozhemiako, Dimitris Mylonas, Jen Q Pan, Michael J Prerau, Susan Redline, and Shaun M Purcell. Sources of Variation in the Spectral Slope of the Sleep EEG. *eNeuro*, 9(5), 22 September 2022. doi: 10.1523/ENEURO.0094-22.2022.

[58] Hiroshi Yokoyama and Keiichi Kitajo. A data assimilation method to track excitation-inhibition balance change using scalp EEG. *Communications Engineering*, 2(1):1–12, 16 December 2023. doi: 10.1038/s44172-023-00143-7.

[59] Juan L Molina, Bradley Voytek, Michael L Thomas, Yash B Joshi, Savita G Bhakta, Jo A Talledo, Neal R Swerdlow, and Gregory A Light. Memantine Effects on Electroencephalographic Measures of Putative Excitatory/Inhibitory Balance in Schizophrenia. *Biological psychiatry. Cognitive neuroscience and neuroimaging*, 5(6): 562–568, June 2020. doi: 10.1016/j.bpsc.2020.02.004.

[60] Madeline M Robertson, Sarah Furlong, Bradley Voytek, Thomas Donoghue, Charlotte A Boettiger, and Margaret A Sheridan. EEG power spectral slope differs by ADHD status and stimulant medication exposure in early childhood. *Journal of neurophysiology*, 122(6):2427–2437, 1 December 2019. doi: 10.1152/jn.00388.2019.

[61] Brendan D Ostlund, Brittany R Alperin, Trafton Drew, and Sarah L Karalunas. Behavioral and cognitive correlates of the aperiodic (1/f-like) exponent of the EEG power spectrum in adolescents with and without ADHD. *Developmental cognitive neuroscience*, 48:100931, April 2021. doi: 10.1016/j.dcn.2021.100931.

[62] Sarah L Karalunas, Brendan D Ostlund, Brittany R Alperin, Mckenzie Figuracion, Hanna C Gustafsson, Erika Michiko Deming, Dan Foti, Dylan Antovich, Jason Dude, Joel Nigg, and Elinor Sullivan. Electroencephalogram aperiodic power spectral slope can be reliably measured and predicts ADHD risk in early development. *Developmental psychobiology*, 64(3):e22228, April 2022. doi: 10.1002/dev.22228.

[63] Ashan Veerakumar, Vineet Tiruvadi, Bryan Howell, Allison C Waters, Andrea L Crowell, Bradley Voytek, Patricio Riva-Posse, Lydia Denison, Justin K Rajendra, Johnathan A Edwards, Kelly R Bijanki, Ki Sueng Choi, and Helen S Mayberg. Field potential 1/f activity in the subcallosal cingulate region as a candidate signal for monitoring deep brain stimulation for treatment-resistant depression. *Journal of neurophysiology*, 122(3): 1023–1035, 1 September 2019. doi: 10.1152/jn.00875.2018.

[64] Mark A Kramer and Catherine J Chu. A general, noise-driven mechanism for the 1/f-like behavior of neural field spectra. *Neural computation*, 36(8):1643–1668, 19 July 2024. doi: 10.1162/neco_a_01682.

[65] Alberto Mazzoni, Henrik Lindén, Hermann Cuntz, Anders Lansner, Stefano Panzeri, and Gaute T Einevoll. Computing the Local Field Potential (LFP) from Integrate-and-Fire Network Models. *PLoS computational biology*, 11(12):e1004584, December 2015. doi: 10.1371/journal.pcbi.1004584.

[66] Haiguang Wen and Zhongming Liu. Separating Fractal and Oscillatory Components in the Power Spectrum of Neurophysiological Signal. *Brain topography*, 29(1):13–26, January 2016. doi: 10.1007/s10548-015-0448-0.

[67] Takeru Matsuda and Fumiyasu Komaki. Time Series Decomposition into Oscillation Components and Phase Estimation. *Neural computation*, 29(2):332–367, February 2017. doi: 10.1162/NECO_a_00916.

[68] Thomas Donoghue, Matar Haller, Erik J Peterson, Paroma Varma, Priyadarshini Sebastian, Richard Gao, Torben Noto, Antonio H Lara, Joni D Wallis, Robert T Knight, Avgusta Shestyuk, and Bradley Voytek. Parameterizing neural power spectra into periodic and aperiodic components. *Nature neuroscience*, 23(12):1655–1665, December 2020. doi: 10.1038/s41593-020-00744-x.

[69] Amanda M Beck, Mingjian He, Rodrigo G Gutierrez, Gladia C Hotan, and Patrick L Purdon. An iterative search algorithm to identify oscillatory dynamics in neurophysiological time series. *bioRxiv*, page 2022.10.30.514422, 12 December 2023. doi: 10.1101/2022.10.30.514422.

[70] Shiang Hu, Zhihao Zhang, Xiaochu Zhang, Xiaopei Wu, and Pedro A Valdes-Sosa. $\xi$-$\pi$: A Nonparametric Model for Neural Power Spectra Decomposition. *IEEE journal of biomedical and health informatics*, 28(5): 2624–2635, May 2024. doi: 10.1109/JBHI.2024.3364499.

[71] Henrik Lindén, Klas H Pettersen, and Gaute T Einevoll. Intrinsic dendritic filtering gives low-pass power spectra of local field potentials. *Journal of computational neuroscience*, 29(3):423–444, December 2010. doi: 10.1007/s10827-010-0245-4.

[72] Brandon J Thio and Warren M Grill. Relative contributions of different neural sources to the EEG. *NeuroImage*, 275:120179, 15 July 2023. doi: 10.1016/j.neuroimage.2023.120179.

[73] Albert Gidon, Timothy Adam Zolnik, Pawel Fidzinski, Felix Bolduan, Athanasia Papoutsi, Panayiota Poirazi, Martin Holtkamp, Imre Vida, and Matthew Evan Larkum. Dendritic action potentials and computation in human layer 2/3 cortical neurons. *Science*, 367(6473):83–87, 3 January 2020. doi: 10.1126/science.aax6239.

[74] Joshua Milstein, Florian Mormann, Itzhak Fried, and Christof Koch. Neuronal shot noise and Brownian 1/f2 behavior in the local field potential. *PloS one*, 4(2):e4338, 3 February 2009. doi: 10.1371/journal.pone.0004338.

[75] Toru Yanagawa, Zenas C Chao, Naomi Hasegawa, and Naotaka Fujii. Large-scale information flow in conscious and unconscious states: an ECoG study in monkeys. *PloS one*, 8(11):e80845, 15 November 2013. doi: 10.1371/journal.pone.0080845.

[76] J H Tinker, F W Sharbrough, and J D Michenfelder. Anterior shift of the dominant EEG rhytham during anesthesia in the Java monkey: correlation with anesthetic potency. *Anesthesiology*, 46(4):252–259, April 1977. doi: 10.1097/00000542-197704000-00005.

[77] André M Bastos, Jacob A Donoghue, Scott L Brincat, Meredith Mahnke, Jorge Yanar, Josefina Correa, Ayan S Waite, Mikael Lundqvist, Jefferson Roy, Emery N Brown, and Earl K Miller. Neural effects of propofol-induced unconsciousness and its reversal using thalamic stimulation. *eLife*, 10, 27 April 2021. doi: 10.7554/eLife.60824.

[78] Emery N Brown, Ralph Lydic, and Nicholas D Schiff. General anesthesia, sleep, and coma. *The New England journal of medicine*, 363(27):2638–2650, 30 December 2010. doi: 10.1056/NEJMra0808281.

[79] Aylin Cimenser, Patrick L Purdon, Eric T Pierce, John L Walsh, Andres F Salazar-Gomez, Priscilla G Harrell, Casie Tavares-Stoeckel, Kathleen Habeeb, and Emery N Brown. Tracking brain states under general anesthesia by using global coherence analysis. *Proceedings of the National Academy of Sciences of the United States of America*, 108(21):8832–8837, 24 May 2011. doi: 10.1073/pnas.1017041108.

[80] Sujith Vijayan, Shinung Ching, Patrick L Purdon, Emery N Brown, and Nancy J Kopell. Thalamocortical mechanisms for the anteriorization of $\alpha$ rhythms during propofol-induced unconsciousness. *The Journal of neuroscience: the official journal of the Society for Neuroscience*, 33(27):11070–11075, 3 July 2013. doi: 10.1523/JNEUROSCI.5670-12.2013.

[81] Michael Murphy, Marie-Aurélie Bruno, Brady A Riedner, Pierre Boveroux, Quentin Noirhomme, Eric C Landsness, Jean-Francois Brichant, Christophe Phillips, Marcello Massimini, Steven Laureys, Giulio Tononi, and Mélanie Boly. Propofol anesthesia and sleep: a high-density EEG study. *Sleep*, 34(3):283–91A, 1 March 2011. doi: 10.1093/sleep/34.3.283.

[82] Alain Destexhe and Michael Rudolph. Extracting information from the power spectrum of synaptic noise. *Journal of computational neuroscience*, 17(3):327–345, 2004. doi: 10.1023/B:JCNS.0000044875.90630.88.

[83] Richard Gao, Ruud L van den Brink, Thomas Pfeffer, and Bradley Voytek. Neuronal timescales are functionally dynamic and shaped by cortical microarchitecture. *eLife*, 9, 23 November 2020. doi: 10.7554/eLife.61277.

[84] Donald L Snyder and Michael I Miller. *Random Point Processes in Time and Space*. Springer New York, 1991. doi: 10.1007/978-1-4612-3166-0.

[85] Richard Gao. Interpreting the electrophysiological power spectrum. *Journal of neurophysiology*, 115(2):628–630, 1 February 2016. doi: 10.1152/jn.00722.2015.

[86] Quentin Perrenoud and Jessica A Cardin. Beyond rhythm - a framework for understanding the frequency spectrum of neural activity. *Frontiers in systems neuroscience*, 17:1217170, 31 August 2023. doi: 10.3389/fnsys.2023.1217170.

[87] Javier Díaz, Hiroyasu Ando, Goeun Han, Olga Malyshevskaya, Xifang Hayashi, Juan-Carlos Letelier, Masashi Yanagisawa, and Kaspar E Vogt. Recovering Arrhythmic EEG Transients from Their Stochastic Interference. *arXiv [q-bio.NC]*, 14 March 2023.

[88] David A Moses, Nima Mesgarani, Matthew K Leonard, and Edward F Chang. Neural speech recognition: continuous phoneme decoding using spatiotemporal representations of human cortical activity. *Journal of neural engineering*, 13(5):056004, October 2016. doi: 10.1088/1741-2560/13/5/056004.

[89] D J Daley and D Vere-Jones. *An Introduction to the Theory of Point Processes*. Springer New York, 2003. doi: 10.1007/b97277.

[90] Pierre Brémaud. *Fourier Analysis and Stochastic Processes*. Springer International Publishing, 2014. doi: 10.1007/978-3-319-09590-5.

[91] Pierre Brémaud. *Point Process Calculus in Time and Space*. Springer International Publishing, 2020. doi: 10.1007/978-3-030-62753-9.

[92] Pierre Brémaud, Laurent Massoulié, and Andrea Ridolfi. Power spectra of random spike fields and related processes. *Advances in applied probability*, 37(4):1116–1146, December 2005. doi: 10.1239/aap/1134587756.

[93] Paul L Nunez and Ramesh Srinivasan. *Electric Fields of the Brain: The Neurophysics of EEG*. Oxford University Press, 2006.

[94] Jason S Sherfey, Salva Ardid, Joachim Hass, Michael E Hasselmo, and Nancy J Kopell. Flexible resonance in prefrontal networks with strong feedback inhibition. *PLoS computational biology*, 14(8):e1006357, August 2018. doi: 10.1371/journal.pcbi.1006357.

[95] V B Mountcastle, W H Talbot, H Sakata, and J Hyvärinen. Cortical neuronal mechanisms in flutter-vibration studied in unanesthetized monkeys. Neuronal periodicity and frequency discrimination. *Journal of neurophysiology*, 32(3):452–484, May 1969. doi: 10.1152/jn.1969.32.3.452.

[96] Kevin Johnston, Joseph F X DeSouza, and Stefan Everling. Monkey prefrontal cortical pyramidal and putative interneurons exhibit differential patterns of activity between prosaccade and antisaccade tasks. *The Journal*

*of neuroscience: the official journal of the Society for Neuroscience*, 29(17):5516–5524, 29 April 2009. doi: 10.1523/JNEUROSCI.5953-08.2009.

[97] Hugo Merchant, Thomas Naselaris, and Apostolos P Georgopoulos. Dynamic sculpting of directional tuning in the primate motor cortex during three-dimensional reaching. *The Journal of neuroscience: the official journal of the Society for Neuroscience*, 28(37):9164–9172, 10 September 2008. doi: 10.1523/JNEUROSCI.1898-08.2008.

[98] Hugo Merchant, Victor de Lafuente, Fernando Peña Ortega, and Jorge Larriva-Sahd. Functional impact of interneuronal inhibition in the cerebral cortex of behaving animals. *Progress in neurobiology*, 99(2):163–178, November 2012. doi: 10.1016/j.pneurobio.2012.08.005.

[99] Eric Kenji Lee, Hymavathy Balasubramanian, Alexandra Tsolias, Stephanie Udochukwu Anakwe, Maria Medalla, Krishna V Shenoy, and Chandramouli Chandrasekaran. Non-linear dimensionality reduction on extracellular waveforms reveals cell type diversity in premotor cortex. *eLife*, 10, 6 August 2021. doi: 10.7554/eLife.67490.

[100] Bartosz Telenczuk, Maria Telenczuk, and Alain Destexhe. A kernel-based method to calculate local field potentials from networks of spiking neurons. *Journal of neuroscience methods*, 344:108871, 1 October 2020. doi: 10.1016/j.jneumeth.2020.108871.

[101] Matti Hämäläinen, Riitta Hari, Risto J Ilmoniemi, Jukka Knuutila, and Olli V Lounasmaa. Magnetoencephalography—theory, instrumentation, and applications to noninvasive studies of the working human brain. *Reviews of modern physics*, 65(2):413–497, 1 April 1993. doi: 10.1103/RevModPhys.65.413.

[102] Claude Bedard, Charlotte Piette, Laurent Venance, and Alain Destexhe. Extracellular and intracellular components of the impedance of neural tissue. *Biophysical journal*, 121(6):869–885, 15 March 2022. doi: 10.1016/j.bpj.2022.02.022.

[103] Claude Bédard and Alain Destexhe. Macroscopic models of local field potentials and the apparent 1/f noise in brain activity. *Biophysical journal*, 96(7):2589–2603, 8 April 2009. doi: 10.1016/j.bpj.2008.12.3951.

[104] Andrei Belitski, Arthur Gretton, Cesare Magri, Yusuke Murayama, Marcelo A Montemurro, Nikos K Logothetis, and Stefano Panzeri. Low-frequency local field potentials and spikes in primary visual cortex convey independent visual information. *The Journal of neuroscience: the official journal of the Society for Neuroscience*, 28(22): 5696–5709, 28 May 2008. doi: 10.1523/JNEUROSCI.0009-08.2008.

[105] Farhan A Khawaja, James M G Tsui, and Christopher C Pack. Pattern motion selectivity of spiking outputs and local field potentials in macaque visual cortex. *The Journal of neuroscience: the official journal of the Society for Neuroscience*, 29(43):13702–13709, 28 October 2009. doi: 10.1523/JNEUROSCI.2844-09.2009.

[106] Theodoros P Zanos, Patrick J Mineault, and Christopher C Pack. Removal of spurious correlations between spikes and local field potentials. *Journal of neurophysiology*, 105(1):474–486, January 2011. doi: 10.1152/jn.00642.2010.

[107] R T Canolty, E Edwards, S S Dalal, M Soltani, S S Nagarajan, H E Kirsch, M S Berger, N M Barbaro, and R T Knight. High gamma power is phase-locked to theta oscillations in human neocortex. *Science*, 313(5793): 1626–1628, 15 September 2006. doi: 10.1126/science.1128115.

[108] J Andrew Henrie and Robert Shapley. LFP power spectra in V1 cortex: the graded effect of stimulus contrast. *Journal of neurophysiology*, 94(1):479–490, July 2005. doi: 10.1152/jn.00919.2004.

[109] Nur Ahmadi, Timothy G Constandinou, and Christos-Savvas Bouganis. Inferring entire spiking activity from local field potentials. *Scientific reports*, 11(1):19045, 24 September 2021. doi: 10.1038/s41598-021-98021-9.

[110] Rishidev Chaudhuri, Biyu J He, and Xiao-Jing Wang. Random Recurrent Networks Near Criticality Capture the Broadband Power Distribution of Human ECoG Dynamics. *Cerebral cortex*, 28(10):3610–3622, 1 October 2018. doi: 10.1093/cercor/bhx233.

[111] Brendan Brady and Tim Bardouille. Periodic/Aperiodic parameterization of transient oscillations (PAPTO)-Implications for healthy ageing. *NeuroImage*, 251:118974, 1 May 2022. doi: 10.1016/j.neuroimage.2022.118974.

[112] Adam M Hughes, Tara A Whitten, Jeremy B Caplan, and Clayton T Dickson. BOSC: a better oscillation detection method, extracts both sustained and transient rhythms from rat hippocampal recordings. *Hippocampus*, 22(6):1417–1428, June 2012. doi: 10.1002/hipo.20979.

[113] Csenge G Horváth, Orsolya Szalárdy, Péter P Ujma, Péter Simor, Ferenc Gombos, Ilona Kovács, Martin Dresler, and Róbert Bódizs. Overnight dynamics in scale-free and oscillatory spectral parameters of NREM sleep EEG. *Scientific reports*, 12(1):18409, 1 November 2022. doi: 10.1038/s41598-022-23033-y.

[114] J Lanzone, M A Colombo, S Sarasso, F Zappasodi, M Rosanova, M Massimini, V Di Lazzaro, and G Assenza. EEG spectral exponent as a synthetic index for the longitudinal assessment of stroke recovery. *Clinical neurophysiology: official journal of the International Federation of Clinical Neurophysiology*, 137:92–101, May 2022. doi: 10.1016/j.clinph.2022.02.022.

[115] Nico Adelhöfer, Theresa Paulus, Moritz Mückschel, Tobias Bäumer, Annet Bluschke, Adam Takacs, Eszter Tóth-Fáber, Zsanett Tárnok, Veit Roessner, Anne Weissbach, Alexander Münchau, and Christian Beste. Increased scale-free and aperiodic neural activity during sensorimotor integration-a novel facet in Tourette syndrome. *Brain communications*, 3(4):fcab250, 27 October 2021. doi: 10.1093/braincomms/fcab250.

[116] Peter Fransson, Marjo Metsäranta, Mats Blennow, Ulrika Åden, Hugo Lagercrantz, and Sampsa Vanhatalo. Early development of spatial patterns of power-law frequency scaling in FMRI resting-state and EEG data in the newborn brain. *Cerebral cortex*, 23(3):638–646, March 2013. doi: 10.1093/cercor/bhs047.

[117] Richard F Serfozo. Semi-stationary processes. *Zeitschrift für Wahrscheinlichkeitstheorie und Verwandte Gebiete*, 23(2):125–132, 1 June 1972. doi: 10.1007/BF00532855.

[118] Anuththara Rupasinghe and Behtash Babadi. Multitaper Analysis of Semi-Stationary Spectra From Multivariate Neuronal Spiking Observations. *IEEE transactions on signal processing: a publication of the IEEE Signal Processing Society*, 68:4382–4396, 2020. doi: 10.1109/TSP.2020.3010197.

[119] Ali Yousefi, Reza Saadati Fard, Uri T Eden, and Emery N Brown. State-Space Global Coherence to Estimate the Spatio-Temporal Dynamics of the Coordinated Brain Activity. *Conference proceedings: ... Annual International Conference of the IEEE Engineering in Medicine and Biology Society. IEEE Engineering in Medicine and Biology Society. Conference*, 2019:5794–5798, July 2019. doi: 10.1109/EMBC.2019.8856634.

[120] Emily P Stephen, Gladia C Hotan, Eric T Pierce, P Grace Harrell, John L Walsh, Emery N Brown, and Patrick L Purdon. Broadband slow-wave modulation in posterior and anterior cortex tracks distinct states of propofol-induced unconsciousness. *Scientific reports*, 10(1):13701, 13 August 2020. doi: 10.1038/s41598-020-68756-y.

[121] Martin Vinck, Renata Batista-Brito, Ulf Knoblich, and Jessica A Cardin. Arousal and locomotion make distinct contributions to cortical activity patterns and visual encoding. *Neuron*, 86(3):740–754, 6 May 2015. doi: 10.1016/j.neuron.2015.03.028.

[122] Somayeh Shahsavarani, David N Thibodeaux, Weihao Xu, Sharon H Kim, Fatema Lodgher, Chinwendu Nwokeabia, Morgan Cambareri, Alexis J Yagielski, Hanzhi T Zhao, Daniel A Handwerker, Javier Gonzalez-Castillo, Peter A Bandettini, and Elizabeth M C Hillman. Cortex-wide neural dynamics predict behavioral states and provide a neural basis for resting-state dynamic functional connectivity. *Cell reports*, 42(6):112527, 27 June 2023. doi: 10.1016/j.celrep.2023.112527.

[123] Hongkun Zhu, Andrew J Michalak, Edward M Merricks, Alexander H C Agopyan-Miu, Joshua Jacobs, Marla J Hamberger, Sameer A Sheth, Guy M McKhann, Neil Feldstein, Catherine A Schevon, and Elizabeth M C Hillman. Spectral-switching analysis reveals real-time neuronal network representations of concurrent spontaneous naturalistic behaviors in human brain. *bioRxiv*, page 2024.07.08.600416, 11 July 2024. doi: 10.1101/2024.07.08.600416.

[124] Fani Deligianni, Maria Centeno, David W Carmichael, and Jonathan D Clayden. Relating resting-state fMRI and EEG whole-brain connectomes across frequency bands. *Frontiers in neuroscience*, 8:258, 28 August 2014. doi: 10.3389/fnins.2014.00258.

[125] Arjan Hillebrand, Gareth R Barnes, Johannes L Bosboom, Henk W Berendse, and Cornelis J Stam. Frequency-dependent functional connectivity within resting-state networks: an atlas-based MEG beamformer solution. *NeuroImage*, 59(4):3909–3921, 15 February 2012. doi: 10.1016/j.neuroimage.2011.11.005.

[126] Richard F Betzel, John D Medaglia, Ari E Kahn, Jonathan Soffer, Daniel R Schonhaut, and Danielle S Bassett. Structural, geometric and genetic factors predict interregional brain connectivity patterns probed by electrocorticography. *Nature biomedical engineering*, 3(11):902–916, November 2019. doi: 10.1038/s41551-019-0404-5.

[127] Carl D Hacker, Abraham Z Snyder, Mrinal Pahwa, Maurizio Corbetta, and Eric C Leuthardt. Frequency-specific electrophysiologic correlates of resting state fMRI networks. *NeuroImage*, 149:446–457, 1 April 2017. doi: 10.1016/j.neuroimage.2017.01.054.

[128] Vladislav Myrov, Felix Siebenhühner, Joonas J Juvonen, Gabriele Arnulfo, Satu Palva, and J Matias Palva. Rhythmicity of neuronal oscillations delineates their cortical and spectral architecture. *Communications biology*, 7(1):405, 3 April 2024. doi: 10.1038/s42003-024-06083-y.

[129] Peter Dayan and Laurence F Abbott. *Theoretical Neuroscience: Computational and Mathematical Modeling of Neural Systems*. MIT Press, 12 August 2005.

[130] Eugene M Izhikevich. *Dynamical Systems in Neuroscience: The Geometry of Excitability and Bursting*. MIT Press, 22 January 2010.

[131] Wulfram Gerstner, Henning Sprekeler, and Gustavo Deco. Theory and simulation in neuroscience. *Science*, 338 (6103):60–65, 5 October 2012. doi: 10.1126/science.1227356.

[132] Daniel Levenstein, Veronica A Alvarez, Asohan Amarasingham, Habiba Azab, Zhe S Chen, Richard C Gerkin, Andrea Hasenstaub, Ramakrishnan Iyer, Renaud B Jolivet, Sarah Marzen, Joseph D Monaco, Astrid A Prinz, Salma Quraishi, Fidel Santamaria, Sabyasachi Shivkumar, Matthew F Singh, Roger Traub, Farzan Nadim, Horacio G Rotstein, and A David Redish. On the Role of Theory and Modeling in Neuroscience. *The Journal of neuroscience: the official journal of the Society for Neuroscience*, 43(7):1074–1088, 15 February 2023. doi: 10.1523/JNEUROSCI.1179-22.2022.

[133] Samuel A Neymotin, Dylan S Daniels, Blake Caldwell, Robert A McDougal, Nicholas T Carnevale, Mainak Jas, Christopher I Moore, Michael L Hines, Matti Hämäläinen, and Stephanie R Jones. Human Neocortical Neurosolver (HNN), a new software tool for interpreting the cellular and network origin of human MEG/EEG data. *eLife*, 9, 22 January 2020. doi: 10.7554/eLife.51214.

[134] Espen Hagen, Solveig Næss, Torbjørn V Ness, and Gaute T Einevoll. Multimodal Modeling of Neural Network Activity: Computing LFP, ECoG, EEG, and MEG Signals With LFPy 2.0. *Frontiers in neuroinformatics*, 12:92, 18 December 2018. doi: 10.3389/fninf.2018.00092.

[135] Pablo Martínez-Cañada, Torbjørn V Ness, Gaute T Einevoll, Tommaso Fellin, and Stefano Panzeri. Computation of the electroencephalogram (EEG) from network models of point neurons. *PLoS computational biology*, 17(4): e1008893, April 2021. doi: 10.1371/journal.pcbi.1008893.

[136] Kael Dai, Sergey L Gratiy, Yazan N Billeh, Richard Xu, Binghuang Cai, Nicholas Cain, Atle E Rimehaug, Alexander J Stasik, Gaute T Einevoll, Stefan Mihalas, Christof Koch, and Anton Arkhipov. Brain Modeling ToolKit: An open source software suite for multiscale modeling of brain circuits. *PLoS computational biology*, 16(11):e1008386, November 2020. doi: 10.1371/journal.pcbi.1008386.

[137] Sergey L Gratiy, Yazan N Billeh, Kael Dai, Catalin Mitelut, David Feng, Nathan W Gouwens, Nicholas Cain, Christof Koch, Costas A Anastassiou, and Anton Arkhipov. BioNet: A Python interface to NEURON for modeling large-scale networks. *PloS one*, 13(8):e0201630, 2 August 2018. doi: 10.1371/journal.pone.0201630.

[138] Pablo Martínez-Cañada, Eduardo Perez-Valero, Jesus Minguillon, Francisco Pelayo, Miguel A López-Gordo, and Christian Morillas. Combining aperiodic 1/f slopes and brain simulation: An EEG/MEG proxy marker of excitation/inhibition imbalance in Alzheimer's disease. *Alzheimer's & dementia: the journal of the Alzheimer's Association*, 15(3):e12477, 1 September 2023. doi: 10.1002/dad2.12477.

[139] Vyassa L Baratham, Maximilian E Dougherty, John Hermiz, Peter Ledochowitsch, Michel M Maharbiz, and Kristofer E Bouchard. Columnar localization and laminar origin of cortical surface electrical potentials. *The Journal of neuroscience: the official journal of the Society for Neuroscience*, 42(18):3733–3748, 4 May 2022. doi: 10.1523/JNEUROSCI.1787-21.2022.

[140] Katharina Glomb, Joana Cabral, Anna Cattani, Alberto Mazzoni, Ashish Raj, and Benedetta Franceschiello. Computational Models in Electroencephalography. *Brain topography*, 35(1):142–161, January 2022. doi: 10.1007/s10548-021-00828-2.

[141] I Apicella, S Scarpetta, L de Arcangelis, A Sarracino, and A de Candia. Power spectrum and critical exponents in the 2D stochastic Wilson-Cowan model. *Scientific reports*, 12(1):21870, 19 December 2022. doi: 10.1038/s41598-022-26392-8.

[142] Giancarlo La Camera. The Mean Field Approach for Populations of Spiking Neurons. *Advances in experimental medicine and biology*, 1359:125–157, 2022. doi: 10.1007/978-3-030-89439-9_6.

[143] Gerhard Werner. Fractals in the nervous system: conceptual implications for theoretical neuroscience. *Frontiers in physiology*, 1:15, 6 July 2010. doi: 10.3389/fphys.2010.00015.

[144] M C Teich, D H Johnson, A R Kumar, and R G Turcott. Rate fluctuations and fractional power-law noise recorded from cells in the lower auditory pathway of the cat. *Hearing research*, 46(1-2):41–52, June 1990. doi: 10.1016/0378-5955(90)90138-f.

[145] S B Lowen, L S Liebovitch, and J A White. Fractal ion-channel behavior generates fractal firing patterns in neuronal models. *Physical review. E, Statistical physics, plasmas, fluids, and related interdisciplinary topics*, 59 (5 Pt B):5970–5980, May 1999. doi: 10.1103/physreve.59.5970.

[146] Steven Bradley Lowen and Malvin Carl Teich. *Fractal-Based Point Processes (Wiley Series in Probability and Statistics)*. Wiley-Interscience, 23 September 2005.

[147] Torbjørn V Ness, Tom Tetzlaff, Gaute T Einevoll, and David Dahmen. On the validity of electric brain signal predictions based on population firing rates. *bioRxiv*, page 2024.07.10.602833, 13 July 2024. doi: 10.1101/2024.07.10.602833.

[148] Espen Hagen, David Dahmen, Maria L Stavrinou, Henrik Lindén, Tom Tetzlaff, Sacha J van Albada, Sonja Grün, Markus Diesmann, and Gaute T Einevoll. Hybrid scheme for modeling local field potentials from point-neuron networks. *Cerebral cortex (New York, N.Y.: 1991)*, 26(12):4461–4496, 26 December 2016. doi: 10.1093/cercor/bhw237.

[149] Maria Teleńczuk, Bartosz Teleńczuk, and Alain Destexhe. Modelling unitary fields and the single-neuron contribution to local field potentials in the hippocampus. *The Journal of physiology*, 598(18):3957–3972, September 2020. doi: 10.1113/JP279452.

[150] Sebastian Vellmer and Benjamin Lindner. Fokker–Planck approach to neural networks and to decision problems. *The European physical journal. Special topics*, 230(14):2929–2949, 1 October 2021. doi: 10.1140/epjs/s11734-021-00172-3.

[151] E N Gilbert and H O Pollak. Amplitude Distribution of Shot Noise. *The Bell System technical journal*, 39(2): 333–350, March 1960. doi: 10.1002/j.1538-7305.1960.tb01603.x.

[152] Espen Hagen, Steinn H Magnusson, Torbjørn V Ness, Geir Halnes, Pooja N Babu, Charl Linssen, Abigail Morrison, and Gaute T Einevoll. Brain signal predictions from multi-scale networks using a linearized framework. *PLOS Computational Biology*, 18(8):e1010353, 12 August 2022.

[153] Federico Tesler, Núria Tort-Colet, Damien Depannemaecker, Mallory Carlu, and Alain Destexhe. Mean-field based framework for forward modeling of LFP and MEG signals. *Frontiers in computational neuroscience*, 16: 968278, 13 October 2022. doi: 10.3389/fncom.2022.968278.

[154] Benjamin Lindner. Superposition of many independent spike trains is generally not a Poisson process. *Physical review. E, Statistical, nonlinear, and soft matter physics*, 73(2 Pt 1):022901, February 2006. doi: 10.1103/PhysRevE.73.022901.

[155] Wulfram Gerstner, Werner M Kistler, Richard Naud, and Liam Paninski. *Neuronal Dynamics: From Single Neurons to Networks and Models of Cognition*. Cambridge University Press, 24 July 2014.

[156] Kyle Q Lepage, Mark A Kramer, and Uri T Eden. The dependence of spike field coherence on expected intensity. *Neural computation*, 23(9):2209–2241, September 2011. doi: 10.1162/NECO_a_00169.

[157] Mark A Kramer and Uri T Eden. *Case Studies in Neural Data Analysis: A Guide for the Practicing Neuroscientist*. MIT Press, 4 November 2016.

[158] Wan-Chi Hsin, Uri T Eden, and Emily P Stephen. Switching Functional Network Models of Oscillatory Brain Dynamics. In *2022 56th Asilomar Conference on Signals, Systems, and Computers*, pages 607–612. IEEE, 31 October 2022. doi: 10.1109/IEEECONF56349.2022.10052077.

[159] P A W Lewis and G S Shedler. Simulation of nonhomogeneous poisson processes by thinning. *Naval research logistics quarterly*, 26(3):403–413, September 1979. doi: 10.1002/nav.3800260304.

[160] Yasuo Nagasaka, Kentaro Shimoda, and Naotaka Fujii. Multidimensional recording (MDR) and data sharing: an ecological open research and educational platform for neuroscience. *PloS one*, 6(7):e22561, 21 July 2011. doi: 10.1371/journal.pone.0022561.

[161] D J Thomson. Spectrum estimation and harmonic analysis. *Proceedings of the IEEE. Institute of Electrical and Electronics Engineers*, 70(9):1055–1096, 1982. doi: 10.1109/proc.1982.12433.

# Supplement 1: Methods for the data example in Figure 1

## Monkey ECoG data

In Figure 1, we analyze and model *Macaca fuscata* monkey ECoG data recorded under propofol anesthesia, where electrode coverage was over the left hemisphere (frontal, parietal, temporal, and occipital lobes). The data (M1) is documented and available in the public server Neurotycho.org [160] and is described experimentally in [75] and surgically in [160]. The monkey was recorded with a sampling rate of 1 kHz for 20 minutes while awake before being infused with 5.2 mg/kg of propofol until loss of behavioral consciousness (LOC). LOC was defined as the time when the monkey did not respond to manipulation of the hand or touching the nostril or philtrum with a cotton swab. Once LOC was established, data were recorded while the monkey was receiving propofol for 10 minutes before the infusion was stopped and the monkey recovered.

## Multitaper spectral analysis

A spectrotemporal estimate of 72 minutes of the recording session was generated using multitaper spectral estimation [161], with time resolution of 30 seconds and a frequency resolution of 2 Hz; the resulting spectrograms were averaged across electrodes (top Figure 1 Panel A). To highlight representative spectra as a function of brain state, an awake average spectrum is shown between 22 and 26 minutes (bottom left Figure 1 Panel A) and a behaviorally unconscious average spectrum is shown between 45 and 49 minutes (bottom right Figure 1 Panel A).

## FPP models of propofol anesthesia-induced unconciousness

The FPP framework was used to generate a forward model of the empirical spectrogram shown in Figure 1 Panel A. Three models were generated, 'awake,' 'anesthetized,' and 'infusion'. As in the original study [75], we focus on the relatively stable dynamics in the 'awake' and 'anesthetized' states.

Awake and anesthetized states were modeled as a bivariate Cox process with AMPA and GABA subprocesses that share a CIF up to a scalar vector, as derived in Equation 28; the additional 1/f-like filter was also used, which distributes across Equation 28 similar to that shown in 25. The CIF is given as a spectrally defined Gaussian process, as in 29, with different rhythmic peaks in each state. The anesthetized model has two narrowband rhythms to capture the well-established slow wave and alpha rhythm. The awake model has a single 'eyes closed' alpha rhythm, but no slow wave.

The 'infusion' state was modeled as independent univariate homogeneous Poisson processes modeling AMPA and GABA with an additional 1/f-like filter.

The parameters for the 'awake', 'infusion', and 'anesthetized' models were chosen by hand-tuning (see Supplemental tables 1-3) so that the overall theoretical spectrum matched the empirical spectrum according to the mean absolute error, while constraining the parameters to create (1) rhythms in the slow and alpha range, and (2) AMPA and GABA waveforms within physiologically realistic ranges. Final model parameters are given in tables 1 (Awake), 2 (Anesthetized), and 3 (Infusion).

# Supplement 2: Model Parameter Tables

| **Awake FFP Model Parameters** | **Value** |
|---|---|
| Rhythm Max Power | 1500.0 $spikes/sec$ |
| Rhythm Center Frequency | 13.0690611 Hz |
| Rhythm Frequency Width | 2.59384288 Hz |
| AMPA $\lambda_0$ | 9777.8253 $spikes/sec$ |
| GABA $\lambda_0$ | 420.672889 $spikes/sec$ |
| Scalar 1 | 977.551196 |
| Scalar 2 | 1000.0 |
| AMPA $\tau_{decay}$ | 3.3 ms |
| GABA $\tau_{decay}$ | 50.0 ms |
| AMPA $\tau_{rise}$ | 0.163508138 ms |
| GABA $\tau_{rise}$ | 0.1 ms |
| Low-pass $\tau_{LP}$ | 80.9611576 ms |

Table 1: Figure 1 Awake State Model Parameters

| **Anesthetized FFP Model Parameters** | **Value** |
|---|---|
| Rhythm Max Power 1 | 2446.87 $spikes/sec$ |
| Rhythm Center Frequency 1 | 0.9604499 Hz |
| Rhythm Frequency Width 1 | 0.75 Hz |
| Rhythm Max Power 2 | 1425.298 $spikes/sec$ |
| Rhythm Center Frequency 2 | 17.21108 Hz |
| Rhythm Frequency Width 2 | 2.0 Hz |
| AMPA $\lambda_0$ | 6767.723 $spikes/sec$ |
| GABA $\lambda_0$ | 336.6484 $spikes/sec$ |
| Scalar 1 | 1750.964 |
| Scalar 2 | 2162.582 |
| AMPA $\tau_{decay}$ | 1.230482 ms |
| GABA $\tau_{decay}$ | 4.838675 ms |
| AMPA $\tau_{rise}$ | 0.2666333 ms |
| GABA $\tau_{rise}$ | 0.2680273 ms |
| Low-pass $\tau_{LP}$ | 7.0 ms |

Table 2: Figure 1 Anesthetized State Model Parameters

| **Infusion FFP Model Parameters** | **Value** |
|---|---|
| AMPA $\lambda_0$ | 22767.5109 $spikes/sec$ |
| GABA $\lambda_0$ | 679.678298 $spikes/sec$ |
| Scalar 1 | 103.742954 |
| Scalar 2 | 243.979565 |
| AMPA $\tau_{decay}$ | 7.99997309 ms |
| GABA $\tau_{decay}$ | 9.81179409 ms |
| AMPA $\tau_{rise}$ | 0.35979477 ms |
| GABA $\tau_{rise}$ | 0.120320066 ms |
| Low-pass $\tau_{LP}$ | 6.54483556 ms |

Table 3: Figure 1 Infusion State Model Parameters

| **Model Parameters** | **Value** |
|---|---|
| Rhythm Max Power | 5000 $spikes/sec$ |
| Rhythm Center Frequency | 1 Hz |
| Rhythm Frequency Width | 0.1 Hz |
| GABA $\lambda_0$ | 500 $spikes/sec$ |
| GABA $\tau_{decay}$ | 10 ms |
| GABA $\tau_{rise}$ | 0.4 ms |
| Low-pass $\tau_{LP}$ | 10 ms |

Table 4: Figure 2 Model Parameters

| **Model Parameters** | **Value** |
|---|---|
| GABA $\lambda_0$ | 150 $spikes/sec$ |
| $\alpha_1$ | 1.9897557323136878 |
| $\alpha_2$ | $-0.9901$ |
| $\sigma^2$ | 0.7 |
| GABA $\tau_{decay}$ | 10 ms |
| GABA $\tau_{rise}$ | 0.4 ms |
| Low-pass $\tau_{LP}$ | 10 ms |

Table 5: Figure 3 One Process Model Parameters

| **Model Parameters** | **Value** |
|---|---|
| GABA $\lambda_0$ | 100 $spikes/sec$ |
| AMPA $\lambda_0$ | 150 $spikes/sec$ |
| $\alpha_1$ | 1.9897557323136878 |
| $\alpha_2$ | $-0.9901$ |
| GABA $\sigma^2$ | 0.315 |
| AMPA $\sigma^2$ | 0.3 |
| GABA $\tau_{decay}$ | 10 ms |
| GABA $\tau_{rise}$ | 0.4 ms |
| AMPA $\tau_{decay}$ | 10 ms |
| AMPA $\tau_{rise}$ | 0.4 ms |
| Low-pass $\tau_{LP}$ | 10 ms |

Table 6: Figure 3 Two Process Model Parameters

| **Parameter** | **Value (Panel A)** | **Value (Panel B)** | **Value (Panel C)** |
|---|---|---|---|
| GABA $\lambda_0$ | 50 $spikes/sec$ | 400 $spikes/sec$ | 50 $spikes/sec$ |
| $\alpha_1$ | 1.9897557323136878 | unchanged | unchanged |
| $\alpha_2$ | $-0.9901$ | unchanged | unchanged |
| $\sigma^2$ | 0.315 | 0.315 | 0.1 |
| GABA $\tau_{decay}$ | 10 ms | unchanged | unchanged |
| GABA $\tau_{rise}$ | 0.4 ms | unchanged | unchanged |
| Low-pass $\tau_{LP}$ | 10 ms | unchanged | unchanged |

Table 7: Figure 4 Model Parameters

| **Model Parameters** | **Value** |
|---|---|
| Rhythm Max Power | 5000 $spikes/sec$ |
| Rhythm Center Frequency | 1 Hz |
| Rhythm Frequency Width | 0.1 Hz |
| AMPA $\lambda_0$ | 500 $spikes/sec$ |
| GABA $\lambda_0$ | 100 $spikes/sec$ |
| Scalar 1 | 1.5 |
| Scalar 2 | -0.8 |
| AMPA $\tau_{decay}$ | 4 ms |
| GABA $\tau_{decay}$ | 10 ms |
| AMPA $\tau_{rise}$ | 0.4 ms |
| GABA $\tau_{decay}$ | 0.4 ms |
| Low-pass $\tau_{LP}$ | 10 ms |

Table 8: Figure 5 Model Parameters

# Supplement 3: Asymptotic (Limiting) Slope Analysis

In this supplement, we perform an asymptotic analysis of the model structure shown in Figure 2 Panel I, focusing on the spectral slope as frequency $f \to \infty$. We start with the functional form of each filter and end with the limiting slope of the power spectrum for each model component.

## 1. Postsynaptic Potential

The Fourier Transform of the Postsynaptic Potential (PSP) filter is given by:

$$H_{\text{PSP}}(f) = \frac{1}{\frac{1}{\tau_{\text{decay}}} + i2\pi f} - \frac{1}{\frac{1}{\tau_{\text{rise}}} + i2\pi f},$$

where $\tau_{\text{decay}}$ and $\tau_{\text{rise}}$ are time constants, and $i = \sqrt{-1}$.

### Step 1.1: Simplify Each Term at High Frequencies

Define:

$$a = \frac{1}{\tau_{\text{decay}}}, \quad b = \frac{1}{\tau_{\text{rise}}}, \quad s = i2\pi f.$$

Then, the functional form becomes:

$$H_{\text{PSP}}(f) = \frac{1}{a+s} - \frac{1}{b+s}.$$

Compute the difference:

$$\begin{aligned} H_{\text{PSP}}(f) &= \frac{1}{a+s} - \frac{1}{b+s} \\ &= \frac{(b+s)-(a+s)}{(a+s)(b+s)} \\ &= \frac{b-a}{(a+s)(b+s)}. \end{aligned}$$

At high frequencies ($f \to \infty$), $|s| \gg a, b$, so:

$$a + s \approx s, \quad b + s \approx s.$$

Thus, the denominator simplifies to:

$$(a+s)(b+s) \approx s \cdot s = s^2.$$

Therefore, the functional form simplifies to:

$$H_{\text{PSP}}(f) \approx \frac{b-a}{s^2}.$$

### Step 1.2: Compute the Magnitude and Square the Expression

Compute the magnitude of $H_{\text{PSP}}(f)$:

$$\begin{aligned} |H_{\text{PSP}}(f)| &= \left| \frac{b-a}{s^2} \right| \\ &= \left| \frac{b-a}{(i2\pi f)^2} \right| \\ &= \left| \frac{b-a}{-(2\pi f)^2} \right| \\ &= \frac{|b-a|}{(2\pi f)^2}, \end{aligned}$$

since $i^2 = -1$ and the magnitude of a real number is its absolute value.

Then, compute the magnitude squared:

$$|H_{\text{PSP}}(f)|^2 = \left(\frac{|b-a|}{(2\pi f)^2}\right)^2 = \frac{C_{\text{PSP}}}{f^4},$$

where:

$$C_{\text{PSP}} = \left(\frac{|b-a|}{(2\pi)^2}\right)^2 = \left(\frac{1}{(2\pi)^2}\left|\frac{1}{\tau_{\text{rise}}} - \frac{1}{\tau_{\text{decay}}}\right|\right)^2.$$

**Step 1.3: Log-Log Slope**

Taking the logarithm:

$$\begin{aligned}\log|H_{\text{PSP}}(f)|^2 &= \log\left(\frac{C_{\text{PSP}}}{f^4}\right)\\ &= \log C_{\text{PSP}} - 4\log f.\end{aligned}$$

Here, we use the logarithm property $\log\left(\frac{A}{B}\right) = \log A - \log B$ and $\log f^4 = 4\log f$.

**Impact on Slope:** The term $\log C_{\text{PSP}}$ is a constant with respect to $f$. **In a log-log plot, the slope is determined by the coefficient of** $\log f$**.** Therefore, the constant term does not affect the slope.

Thus, the slope of $|H_{\text{PSP}}(f)|^2$ in the log-log domain is:

$$\boxed{\text{Spectral Slope of } |H_{\text{PSP}}(f)|^2 = -4.}$$

**2. Low-Pass Filter (LP)**

The low-pass filter functional form is given by:

$$H_{\text{LP}}(f) = \frac{1}{1 + i2\pi f\tau_{\text{LP}}},$$

where $\tau_{\text{LP}}$ is the time constant of the low-pass filter.

**Step 2.1: Simplify at High Frequencies**

At high frequencies ($f \to \infty$), the term $i2\pi f\tau_{\text{LP}}$ dominates the denominator:

$$1 + i2\pi f\tau_{\text{LP}} \approx i2\pi f\tau_{\text{LP}}.$$

Therefore, the functional form simplifies to:

$$H_{\text{LP}}(f) \approx \frac{1}{i2\pi f\tau_{\text{LP}}}.$$

**Step 2.2: Compute the Magnitude and Square the Expression**

Compute the magnitude:

$$\begin{aligned}|H_{\text{LP}}(f)| &= \left|\frac{1}{i2\pi f\tau_{\text{LP}}}\right|\\ &= \frac{1}{2\pi f\tau_{\text{LP}}},\end{aligned}$$

since $|i| = 1$.

Then, compute the magnitude squared:

$$|H_{\text{LP}}(f)|^2 = \left(\frac{1}{2\pi f\tau_{\text{LP}}}\right)^2 = \frac{C_{\text{LP}}}{f^2},$$

where:

$$C_{\text{LP}} = \left(\frac{1}{2\pi\tau_{\text{LP}}}\right)^2.$$

**Step 2.3: Log-Log Slope**

Taking the logarithm:

$$\begin{aligned}\log |H_{\text{LP}}(f)|^2 &= \log \left( \frac{C_{\text{LP}}}{f^2} \right) \\ &= \log C_{\text{LP}} - 2 \log f.\end{aligned}$$

Here, we use $\log \left( \frac{A}{B} \right) = \log A - \log B$ and $\log f^2 = 2 \log f$.

**Impact on Slope:** The constant term $\log C_{\text{LP}}$ does not affect the slope. The slope is determined by the $-2 \log f$ term. Thus, the slope of $|H_{\text{LP}}(f)|^2$ in the log-log domain is:

$$\boxed{\text{Spectral Slope of } |H_{\text{LP}}(f)|^2 = -2.}$$

**3. Point Process Spectrum.**

The Cox point process spectrum, which includes both rhythmic (e.g., Gaussian) and broadband (constant rate) components, is given by:

$$S_x(f) = S_\lambda(f) + \lambda_0,$$

where $S_\lambda(f)$ represents the conditional intensity function (CIF), and $\lambda_0$ is the rate of the process, representing a flat spectrum.

As an example of a CIF for the process, we use a spectrally defined Gaussian process where the shape of the power spectrum is defined as a Gaussian bump given by:

$$S_\lambda(f) = A_i \exp \left( -\frac{(f - \mu_i)^2}{2\sigma_i^2} \right),$$

where $A_i$, $\mu_i$, and $\sigma_i$ are constants.

**Step 3.1: Asymptotic Behavior at High Frequencies**

As $f \to \infty$, the Gaussian component $S_\lambda(f)$ decays exponentially to zero:

$$\lim_{f \to \infty} S_\lambda(f) = A_i \exp \left( -\frac{(f - \mu_i)^2}{2\sigma_i^2} \right) \to 0.$$

Therefore, at high frequencies, the Gaussian term $S_\lambda(f)$ contributes negligibly to the spectrum relative to the non-zero constant broadband component. However, the slope of $S_\lambda(f)$ will not be strictly zero in log-log.

**Step 3.2: Log-Log Slope**

$S_\lambda(f)$ decays (exponentially) faster than any linear rate in log-log space. As such, its limiting slope is:

$$\boxed{\text{Spectral Slope of } S_\lambda(f) = -\infty.}$$

Even though the limiting slope is non-zero because of the exponential decay, the Gaussian component will not contribute to the overall model limiting slope because, relative to the broadband component, $S_\lambda(f)$ is not contributing much to the spectrum at high frequencies. Because the remaining term is a constant, the slope from $\lambda_0$ is 0. Thus, the spectral slope of the point process spectrum $S_x(f)$ at high frequencies is:

$$\boxed{\text{Spectral Slope of } S_x(f) = 0.}$$

**Note:** It's important to note that while $S_\lambda(f)$ decays to zero exponentially fast, $\lambda_0$ remains constant. There are scenarios where the spectral slope of $S_x(f)$ might not be zero, which would occur when the rhythmic component $S_\lambda(f)$ would dominate over the broadband component $\lambda_0$ at high frequencies (i.e., the spectrum decays at a rate slower than linear in log-log space).

### 4. Full Combined Model

The full combined model is:

$$S_{\text{combined}}(f) = |H_{\text{PSP}}(f)|^2 \times |H_{\text{LP}}(f)|^2 \times [S_x(f)]\,.$$

**Step 4.1: Asymptotic Behavior at High Frequencies**

Using the asymptotic forms from previous sections:

$$|H_{\text{PSP}}(f)|^2 \approx \frac{C_{\text{PSP}}}{f^4}, \quad |H_{\text{LP}}(f)|^2 \approx \frac{C_{\text{LP}}}{f^2}, \quad [S_x(f)] \approx \lambda_0.$$

Therefore, at high frequencies:

$$S_{\text{combined}}(f) \approx \frac{C_{\text{PSP}}}{f^4} \times \frac{C_{\text{LP}}}{f^2} \times \lambda_0 = \lambda_0 C_{\text{PSP}} C_{\text{LP}} \cdot \frac{1}{f^6}.$$

**Step 4.2: Log-Log Slope**

Taking the logarithm:

$$\begin{aligned}\log S_{\text{combined}}(f) &= \log\left(\lambda_0 C_{\text{PSP}} C_{\text{LP}} \cdot f^{-6}\right)\\ &= \log(\lambda_0 C_{\text{PSP}} C_{\text{LP}}) + \log f^{-6}\\ &= \log(\lambda_0 C_{\text{PSP}} C_{\text{LP}}) - 6\log f.\end{aligned}$$

Here, we use the logarithm properties $\log(AB) = \log A + \log B$ and $\log f^{-6} = -6\log f$.

**Impact on Slope:** The constant term $\log(\lambda_0 C_{\text{PSP}} C_{\text{LP}})$ does not depend on $f$ and thus does not affect the slope. **The slope is determined solely by the $-6\log f$ term.**

Thus, the spectral slope of the full combined model at high frequencies is:

$$\boxed{\text{Spectral Slope of the full combined model} = -6.}$$

**Summary**

This asymptotic analysis demonstrates that at high frequencies ($f \to \infty$), the spectral slope of the full combined model is determined by the sum of the slopes of the individual filter components and the point process spectrum. Specifically:

$$\text{Total Spectral Slope} = \underbrace{(-4)}_{\text{PSP Filter}} + \underbrace{(-2)}_{\text{LP Filter}} + \underbrace{0}_{\text{Point Process}} = \boxed{-6}$$

This style of limiting slope analysis can be applied to any set of model components that have an analytical solution (e.g., event/additional filters, point processes).

## Supplement 4: Full Gabor Fourier transform with scaling constant

$$\begin{aligned}\mathcal{H}(f) = k \cdot \sigma\sqrt{\frac{\pi}{2}}\Bigg[&\exp\left(-\frac{\sigma^2}{2}\left(\omega + 2\pi f_0\right)^2 - i\left(\theta + t_0\omega\right)\right)\\ &+ \exp\left(-\frac{\sigma^2}{2}\left(\omega - 2\pi f_0\right)^2 + i\left(\theta - t_0\omega\right)\right)\Bigg]\end{aligned} \tag{36}$$

where

- $\omega = 2\pi f$ – Angular frequency,
- $k$ – Amplitude scaling factor,
- $f_0$ – Center frequency,
- $\sigma$ – Standard deviation of the Gaussian envelope,
- $\theta$ – Phase offset,
- $t_0$ – Time shift.